European Journal of Mechanics / A Solids 106 (2024) 105295

Contents lists available at ScienceDirect

European Journal of Mechanics / A Solids

journal homepage: www.elsevier.com/locate/ejmsol

Full length article

Calibrating failure surfaces for vertically perforated clay block masonry using a validated numerical unit cell model

Raphael Reismüller [a,*], Markus Lukacevic [a], Sebastian Pech [a], Andreas Jäger [b], Josef Füssl [a]

[a] Institute for Mechanics of Materials and Structures, TU Wien, Karlsplatz 13/202, 1040, Vienna, Austria
[b] Wienerberger AG, Wienerbergerplatz 1, 1100, Vienna, Austria

ARTICLE INFO

Keywords:
Unit cell
Vertically perforated clay block
Finite element method
Masonry
Failure surfaces
In-plane loading
XFEM

ABSTRACT

Finite element software is nowadays an essential part of a structural engineer's modeling process. The simulations range from trivial linear elastic models to highly non-linear ones, accounting for contact, plasticity, viscoelasticity, or fracture. Though fired clay blocks are an excellent and widely used building material, little effort has been made to extend available failure surfaces for simulating vertically perforated clay block masonry in modern FE Software. Therefore, developing reliable and efficient ways to predict the effective strength of vertically perforated clay block masonry subjected to different loading states is critical. In this study, we aim to qualitatively analyze the failure surface of vertically perforated clay block masonry under in-plane loading, using numerical simulations. Using a previously validated unit cell FE model, we derived the peak stresses from 471 simulations. Subsequently, we compared these results with two failure surfaces from the literature and identified qualitative differences. Taking these differences into account, we propose a concept for numerically calibrating the parameters of the Rankine–Hill failure surface proposed by Lourenço (1997).

1. Introduction

Clay block masonry is one of the oldest building materials in human history and has been used for many centuries. Especially in Central Europe, it is still a popular building material for its low thermal conductivity, durability, fire resistance, and ease of construction. Additionally, mainly abundant natural materials are used for the production of clay blocks, which makes them a sustainable building material (Pohl, 2020). Today, mostly vertically perforated clay blocks are used for structural clay block masonry. A typical vertically perforated clay block design consists of a network of slender, plate-like webs, which are mostly oriented orthogonal to each other (see Fig. 1). These webs can be categorized by their orientation: *longitudinal webs* are oriented parallel to the wall surface and *transversal webs* are oriented perpendicular to the wall surface.

In the last decades, masonry has fallen behind other building materials like concrete or steel. This has several reasons: (i) Fired clay fails very brittle and the material properties show large fluctuations since the raw material is a natural product and the production process is not fully controllable. Additionally, the combination of clay blocks and mortar results in a heterogeneous material system, which requires sophisticated homogenization strategies for macroscale simulations. (ii) Block designs, joint types, and bond types are extremely diverse, which makes it difficult to find a general approach for the calculation of clay block masonry. (iii) The maximum strength properties of vertically perforated clay block masonry are typically smaller than those of concrete and steel. Hence, the use of vertically perforated clay block masonry is out of question for high-rise buildings. (iv) The structural system of clay block masonry is very different from the structural systems of other building materials. While steel and concrete structures, can be deconstructed into beams, pillars, and trusses, clay block masonry structures typically consist of plates. A structure's behavior consisting of many plates is harder to grasp than the behavior of beam-and-pillar structures. Thus, although used for so long, masonry has nowadays a subordinate role when thinking of larger buildings.

Modern FE software is massively simplifying the calculation of complex buildings and a rapidly growing number of structural engineers rely on numerical simulations in the design process. In these numerical simulations, the structural components are considered homogeneous continua with effective material properties. Therefore, reliable macroscopic failure surfaces are necessary for assessing the load-bearing capacity of a structure. While failure criteria for concrete and steel are well established in FE software, this is not the case for masonry. Thus, the implementation of a reliable failure surface for masonry is necessary to keep up with other building materials.

In the last five decades, many studies on different macroscopic material models for masonry were published (Hegemier et al., 1978;

* Corresponding author.
E-mail address: raphael.reismueller@tuwien.ac.at (R. Reismüller).

https://doi.org/10.1016/j.euromechsol.2024.105295
Received 1 December 2023; Received in revised form 6 March 2024; Accepted 7 March 2024
Available online 11 March 2024

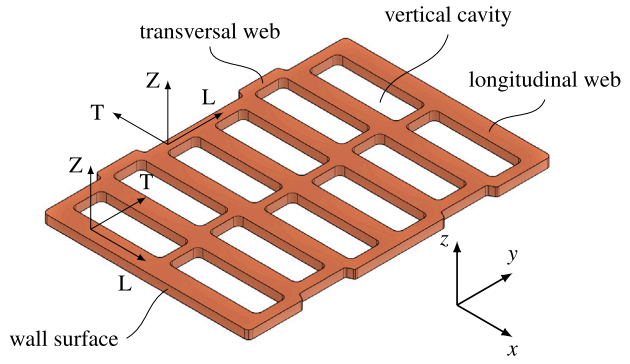

Fig. 1. Parts of a vertically perforated clay block and material orientation represented by the L-T-Z coordinate system.
Source: From Reismüller et al. (2023a).

Hendry, 1978; Hamid and Drysdale, 1981; Page, 1981; Mann and Müller, 1982; Ganz, 1985; Essawy and Drysdale, 1986; Wan and Yi, 1986; Dialer, 1990; Vratsanou, 1992; Seim, 1995; Andreaus, 1996; Lourenço, 1996; Lourenço et al., 1997; Schlegel and Rautenstrauch, 2000; Zilch and Schermer, 2003; Mojsilović, 2011). Two of these models became established in the scientific community for their unique prediction qualities and their applicability for vertically perforated clay block masonry: the multi-surface criterion developed by Ganz (1985) and the Rankine–Hill surface proposed by Lourenço et al. (1996, 1997). Examples for their application can be found in Rudisch et al. (2017), Lang and Bachmann (2003), Mistler et al. (2006), Seim and Pfeiffer (2011), Kotze et al. (2019), Netzel and Van Zijl (2004), Grande et al. (2013, 2008), Van Den Heever et al. (2021) and Da Porto et al. (2010). Especially the Rankine–Hill surface is well suited for implementation in FE software and some developers already implemented it into their software (e. g. Dlubal Software GmbH, 2020) Thus, the problem is not the lack of failure surfaces, but the calibration of these surfaces for a specific masonry product.

Typically, three different experimental series are carried out for deriving the strength parameters of a masonry product: uniaxial vertical compression tests on single blocks (EN 772-1, 2016), uniaxial vertical compression tests on larger wall specimens (EN 1052-1, 1998), and shear tests on specimens consisting of two or three blocks (EN 1052-3, 2002). Since the failure mechanism of a single block under compression is very different from the failure mechanism of a wall specimen under vertical compression (Suda et al., 2021; Reismüller et al., 2023b), the strength parameters from single block tests cannot be used for calibrating macroscopic material properties. Hence, only two different experimental series are generally available for calibrating a macroscopic failure surface without doing any additional tests, whereas Lourenço et al. suggests at least seven experiments on wall specimens (refer to Section 2.2). Additionally, uniaxial tensile tests on wall specimens are typically not carried out, since these tests are difficult to perform (see e. g. Ganz and Thürlimann (1982)) and the tensile strength is very low compared to the compressive strength (Page, 1983). Therefore, the tensile strength of masonry is often neglected, which is a very critical assumption, since it can be crucial under shear loading e. g. in earthquake regions.

Using computational methods for predicting the behavior of masonry is getting more and more attention (Leonetti et al., 2018; Bošnjak et al., 2020; Scacco et al., 2020; Segura et al., 2021; Suda et al., 2021; Gaetano et al., 2022; Scacco et al., 2022; Zhou et al., 2022). Since the computational effort is much lower than for experimental tests, numerical simulations are a good alternative for calibrating a macroscopic failure surface. Thus, we developed and validated a numerical model for the simulation of vertically perforated clay block masonry under arbitrary in-plane loading (Reismüller et al., 2023b). Using a unit cell model with periodic boundary conditions (PBC) in combination with the eXtended Finite Element Method (XFEM) (Belytschko and Black, 1999) and the orthotropic Hoffman criterion (Hoffman, 1967) we were able to replicate the failure mechanisms of seven experiments on vertically perforated clay block walls (Bitterli, 2014; Salmanpour, 2017).

Although the surfaces were recently implemented in FE software, a critical gap in the research is still the lack of comprehensive validation for modern vertically perforated clay block masonry. This is primarily due to the sparse availability of experimental data in the literature, which also fails to encompass the full spectrum of loading conditions. This is understandable, considering the substantial effort associated with conducting biaxial experiments on vertically perforated block masonry. Consequently, this lack of empirical validation underscores the pressing need for an alternative approach to comprehensively assess the failure behavior of these modern masonry structures.

Thus, the main aim of the present work is to qualitatively analyze the failure surface of vertically perforated clay block masonry over the entire domain of loading conditions, using the previously validated model. Building on this qualitative analysis, we also aim to provide a concept for calibrating the Rankine–Hill surface for any vertically perforated clay block design. Therefore, we simulate 150 different loading combinations for three different head joint types. To keep the computational effort manageable, we use a simplified block design, which is still able to replicate the typical failure mechanisms of vertically perforated clay block masonry. In doing so, we compare the numerical results to existing failure surfaces to work out similarities, emphasize differences, and provide a concept for using our numerical approach to generate a failure surface for any vertically perforated clay block design.

First, we developed a simplified block design and defined the interface parameters for three typical head joint types: mortared joints, frictional contact, and no contact. Next, we randomly generated 150 different loading combinations using Latin Hypercube Sampling (LHS) (McKay et al., 1979) and simulated them for each head joint type, using the previously validated numerical model. From each of these simulations, we obtained a peak stress state and a governing failure mechanism. Combining this data, we were able to derive a failure surface for each head joint type and define regions with similar failure mechanisms. Afterwards, we compared the results to the failure surfaces proposed by Ganz (1985) and Lourenço et al. (1996, 1997). By doing so, we were able to pinpoint differences between the failure surfaces and the numerical results. For assessing these differences, we next applied the approach to two real block designs. Finally, we gathered the obtained insights to provide a concept for generating a failure surface for any vertically perforated clay block design using our numerical model.

In Section 2, we provide a brief summary of the two most common failure surfaces for fired clay block masonry. Section 3 contains an overview of the applied modeling strategies and the numerical model. Afterward, we explain and discuss the results in Section 4, followed by our conclusions in Section 5.

2. Failure surfaces for vertically perforated clay block masonry

As stated in the introduction, for the simulation of entire masonry buildings in FE software we need the homogenized elastic properties of masonry and a homogenized failure surface. We refer to the homogenized properties of the wall as *macroscopic* properties. In this manner, we distinguish between two scales of observation: the *macroscopic scale* and the *mesoscopic scale*. On the mesoscopic scale both the clay blocks and the mortar joints are considered separately, while on the macroscopic scale, the masonry wall is considered as a homogeneous continuum (see Fig. 2).

Within this work we focus on the in-plane behavior of masonry, assuming a plane stress state, and considering only axial and shear loading as a simplification.

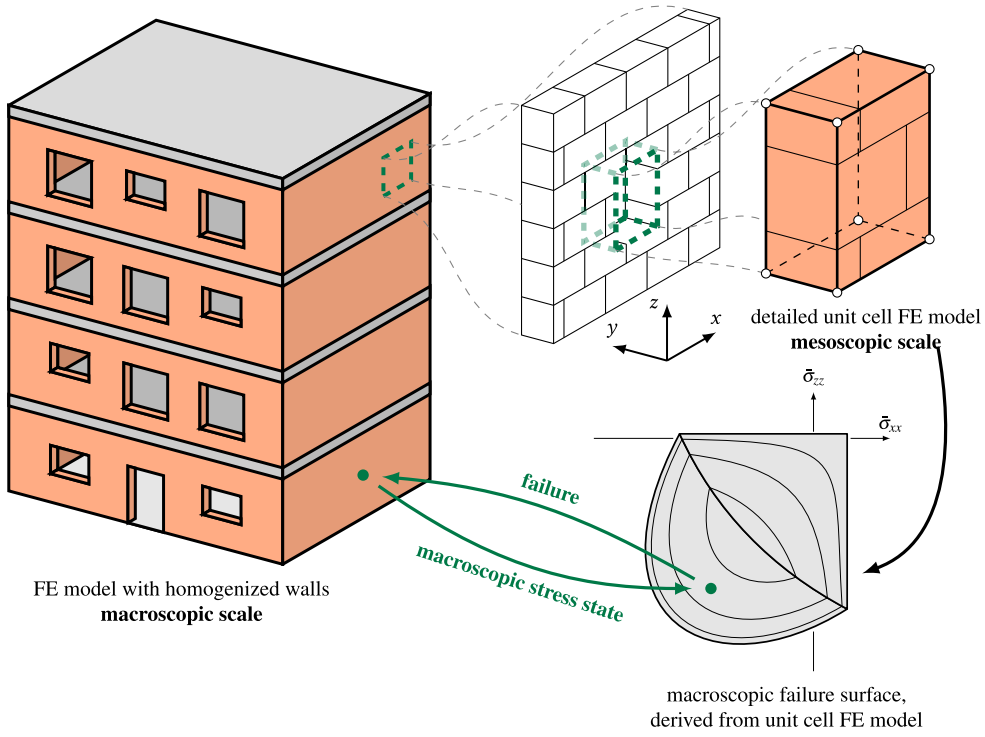

Fig. 2. Meso-to-macro homogenization.

Macroscopic in-plane failure surfaces describe failure under a given stress state $\bar{\sigma}_{xx}$, $\bar{\sigma}_{zz}$, and $\bar{\sigma}_{xz}$. We define the x-axis as horizontal, the z-axis as vertical, and the y-axis as perpendicular to the wall surface (see Figs. 1 and 2).

The two most commonly used macroscopic in-plane failure surfaces, which are also suitable for modern vertically perforated clay block masonry, are the failure surface proposed by Ganz (1985) and the Rankine–Hill surface proposed by Lourenço et al. (1996, 1997). For clarifying the differences between these two failure surfaces, we briefly summarize them in the following sections. While the failure surface of Ganz (1985) consists of twelve criteria (shown in Appendix A), derived from different failure mechanisms observed in block masonry, the Rankine–Hill surface (Lourenço, 1996; Lourenço et al., 1997) has only two criteria (shown in Appendix B), which do not depict any failure mechanisms, but they qualitatively describe the overall shape of the in-plane failure envelope. To carve out similarities and differences between these models, they are briefly summarized in the following sections.

2.1. Failure surface according to Ganz

Ganz (1985) examined three different cases: masonry without tensile strength, reinforced masonry, and masonry with tensile strength. For transferring shear loads under low vertical compression the tensile strength of the mortar joints is crucial. Thus, to utilize the whole potential of the material and to compete with modern building materials, we focused on masonry with tensile strength.

Based on mechanical considerations and typical failure mechanisms, Ganz (1985) formulated a macroscopic failure surface from a combination of mesoscopic material parameters and geometric parameters as well as macroscopic material strengths. Considering both block failure and joint failure, Ganz (1985) derived twelve failure criteria, resulting in a complex failure surface with many intersections (see Fig. 3a). The failure surface is uniquely capable of predicting the governing failure mechanism for different in-plane stress states, however, the post-peak behavior is not accounted for.

For calibrating the failure surface, the following ten parameters are necessary: the horizontal compressive masonry strength $f_{\mathrm{m},x}$, the vertical compressive masonry strength $f_{\mathrm{m},z}$, the vertical tensile masonry strength $f_{\mathrm{t},z}$, the ratio of the fired clay's tensile strength to its compressive strength ω_{m}, the tensile mortar strength $f'_{\mathrm{t},z}$, a parameter μ for defining the horizontal uniaxial compressive strength considering joint failure, the joint's cohesion stress c, the joint's angle of friction φ, the head joint distance a_{S}, and the bed joint distance a_{L}. For a detailed description of the parameters, we refer to the original publication (Ganz, 1985). The definition of the failure surface can be found in Appendix A.

2.2. Rankine–hill failure surface according to Lourenço

The anisotropic Rankine–Hill failure surface, proposed by Lourenço et al. (1996, 1997), consists of two different yield surfaces: a Rankine-type yield surface for tensile failure and a Hill-type yield surface for compressive failure (see Fig. 3b). Instead of deriving failure criteria from failure mechanisms as Ganz (1985) did, Lourenço et al. (1996, 1997) defined phenomenological surfaces for the in-plane failure envelope of masonry. Thus, the model is not capable of distinguishing different failure mechanisms. However, it is much easier to implement into FE software and can account for post-peak behavior. Thereby, an exponential softening is used for the Rankine-type surface and a combination of a parabolic hardening with an exponential softening for the Hill-type surface, which was experimentally shown by Van der Pluijm (1999) for tension and, e. g., Jafari et al. (2019) for compression.

In this work, we only focused on computing the peak stress. Thus, while Lourenço et al. often refers to the equivalent compressive yield stress $\bar{\sigma}_{\mathrm{c},i}\left(\kappa_{\mathrm{c}}\right)$ and the equivalent tensile yield stresses $\bar{\sigma}_{\mathrm{t},i}\left(\kappa_{\mathrm{t}}\right)$, depending on the compressive and tensile softening parameters κ_{c} and κ_{t}, we substitute these terms with the corresponding material strengths $f_{\mathrm{m},i}$ and $f_{\mathrm{t},i}$, considering the softening parameters to be $\kappa_{\mathrm{c}} = 0$ and $\kappa_{\mathrm{t}} = 0$. The definition of the Rankine–Hill surface can be found in Appendix B.

The Rankine–Hill surface is calibrated for a specific masonry by the following seven parameters: (i) the horizontal tensile masonry strength

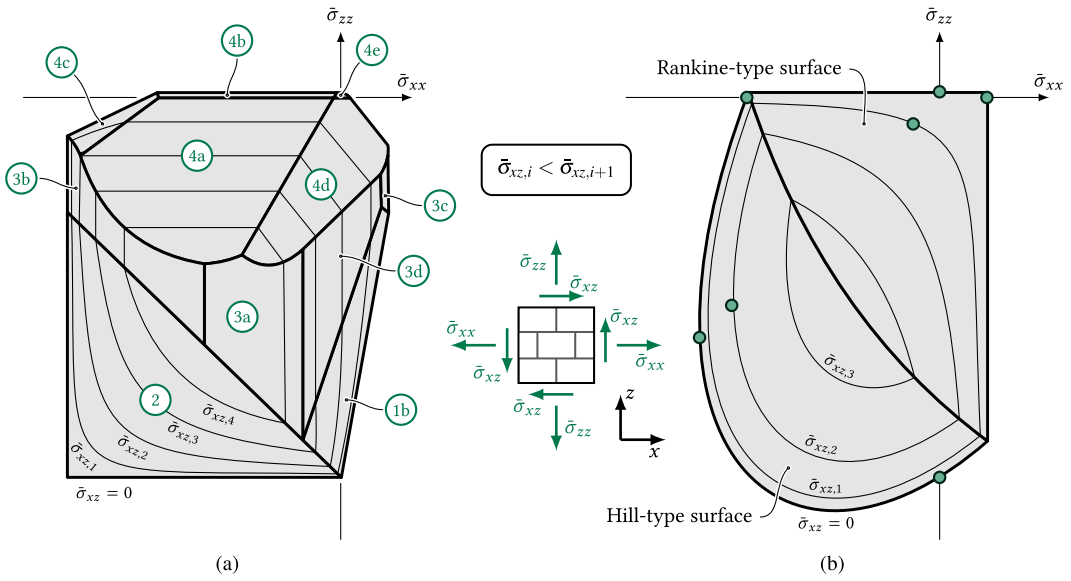

Fig. 3. Most commonly used macroscopic in-plane failure surfaces for masonry: (a) Failure Surface proposed by Ganz (1985) and (b) Rankine–Hill surface proposed by Lourenço et al. (1996, 1997). The numbers in (a) refer to the failure criteria in Appendix A.

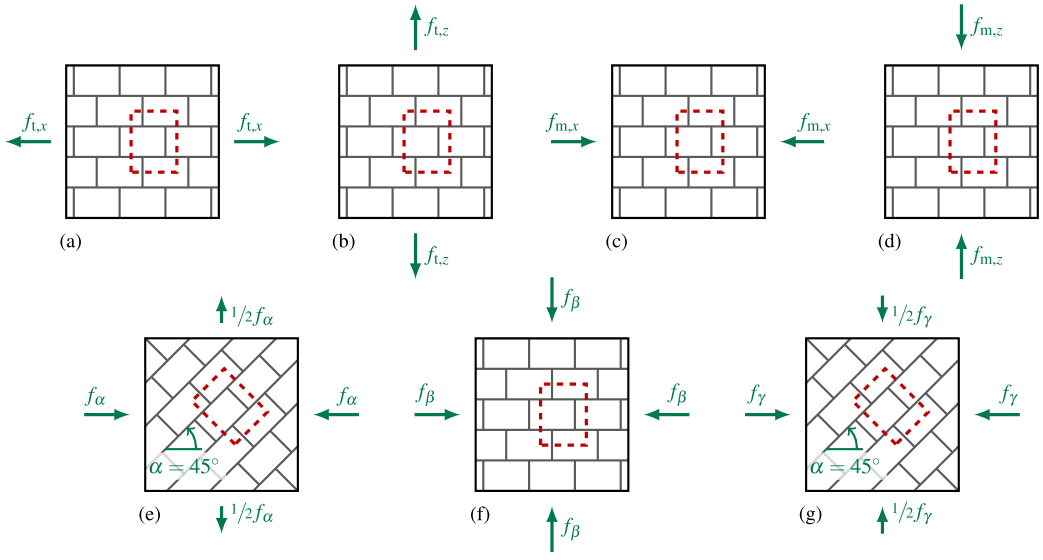

Fig. 4. Loading states proposed by Lourenço et al. (1996, 1997). The red dashed line represents the outline of the chosen repeating unit cell described in Section 3.2.

$f_{t,x}$, (ii) the vertical tensile masonry strength $f_{t,z}$, (iii) the horizontal compressive masonry strength $f_{m,x}$, (iv) the vertical compressive masonry strength $f_{m,z}$, (v) a parameter α for defining the shear strength amount under small axial compressive stresses, (vi) a parameter β for defining the biaxial compressive strength, and (vii) a parameter γ for defining the shear strength amount under large axial compressive stresses. Lourenço et al. (1996, 1997) suggests an ideal set of seven different loading states (see Fig. 4) to obtain the parameter values by a least squares regression. Additional loading states improve the quality of the fit, especially in regions of transitions between failure mechanisms.

3. Numerical model and simulation program

This study mainly focuses on an FE simulation-based characterization of a macroscopic in-plane failure surface for clay block masonry, which also captures the occurring failure mechanisms. This process requires simulating a vast amount of different model configurations. Thus, we designed a simplified but computationally efficient FE model, which can still realistically predict the failure mechanisms and the ultimate strength of clay block masonry. We derived our numerical model from Kiefer et al. (2017) and Suda et al. (2021) and extended it to account for joint failure. We already used and validated the model for different in-plane loading combinations in Reismüller et al. (2023b). Using a unit cell approach with PBCs and a simplified block geometry allowed us to use computationally demanding non-linear models like XFEM for modeling cracks in the fired clay and a cohesive interface damage model for considering joint failure. In the following sections, these modeling strategies are explained in detail, beginning with the geometric definition of the FE model, followed by a discussion of the chosen material behavior and simulation techniques.

3.1. Simplified geometry

Since detailed and sophisticated modeling techniques result in long simulation times (for real block geometries up to 24 h per simulation with 8 CPUs), we developed a simplified geometry, which is still able to reproduce the typical failure mechanisms of vertically perforated

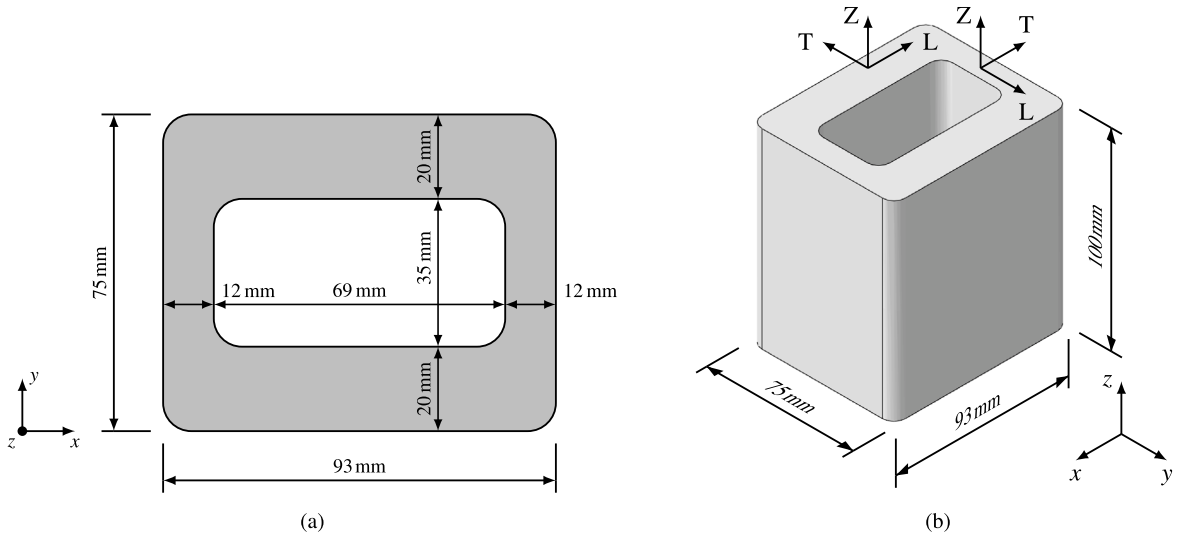

Fig. 5. Simplified geometry of a vertically perforated clay block.

clay blocks. The simplified block geometry consists of two longitudinal as well as two transversal webs (see Fig. 5) and has a void ratio of 35%. Each block is 93 mm long, 75 mm wide, and 100 mm high. Using this design, the simulation times could be reduced to approximately one-tenth of the larger simulations.

3.2. Unit cell concept

The unit cell concept used for the meso-to-macro homogenization utilizes repeating patterns in structures, the so-called *repeating unit cell*. In masonry with a regular running bond, the smallest possible repeating unit cell, without considering symmetric properties, is two blocks high and one block wide with two-dimensional periodicity in x- and z-direction (see Fig. 6a). As long as the unit cell is large enough to capture the characteristic failure mechanisms of the material, the results are representative for the entire structure. Although the results do not depend on the unit cell geometry, choosing a cuboid unit cell considerably simplifies the meshing process and the application of PBCs. We refer to the surfaces of the repeating unit cell as $North$, $South$, $East$, $West$, Top, and $Bottom$, and to the eight vertices according to the surfaces intersecting in this corner (e. g., NWB or SET).

In combination with PBCs, the repeating unit cell behaves as if it was part of an infinitely large wall. Thus, the unit cell concept drastically reduces the numerical effort, compared to simulating a larger structure. The PBCs are linear equations, which couple the displacements of each node on a periodic surface to the displacements of a corresponding node on the opposing surface (i. e., surfaces $East$–$West$ and $North$–$South$), and to the displacements of the primary nodes located in the corners of the repeating unit cell. These equations are shown in detail in Suda et al. (2021).

Since each node pair is coupled to the deformation difference of the primary nodes, we can impose different macroscopic strain states by simply imposing displacements on the primary nodes. We derived these primary node displacements by superposition of the three load cases in Table 1.

3.3. FE model and mesh

Now that we have defined the geometric boundary conditions, we will move on to the modeling in the FE program Abaqus Version 2022HF2. We used a simplified micro-modeling approach, meaning, that the blocks are modeled in full detail, while the joints are reduced to an interface with no thickness (Lourenço, 1996; Lourenço et al., 1997). Thus, the FE model only consists of six fired clay parts, which are connected by interface couplings in the head joint and the bed joint. We distributed the thickness of the mortar joints to the adjacent blocks to maintain the overall dimensions of the repeating unit cell. The mesh consists of 23 978 nodes and 18 540 C3D8 elements and is shown in Fig. 6a. We derived the displacement boundary conditions for each loading combination from the equations in Table 1.

Table 1
Primary node displacements for imposing effective macroscopic strain states.
Source: From Reismüller et al. (2023b).

	Strain state	Primary node displacement
LC1	$\begin{bmatrix} \bar{\varepsilon}_{xx} & 0 \\ 0 & 0 \end{bmatrix}$	*Horizontal uniaxial strain* $u_x^{SEB} = \bar{\varepsilon}_{xx} \cdot l_x, \quad u_x^{SET} = \bar{\varepsilon}_{xx} \cdot l_x$
LC2	$\begin{bmatrix} 0 & 0 \\ 0 & \bar{\varepsilon}_{zz} \end{bmatrix}$	*Vertical uniaxial strain* $u_z^{NWB} = \bar{\varepsilon}_{zz} \cdot l_z, \quad u_z^{NWT} = \bar{\varepsilon}_{zz} \cdot l_z$
LC3	$\begin{bmatrix} 0 & \bar{\varepsilon}_{xz} \\ \bar{\varepsilon}_{xz} & 0 \end{bmatrix}$	*Pure shear strain* $u_z^{SEB} = \bar{\varepsilon}_{xz} \cdot l_x, \quad u_z^{SET} = \bar{\varepsilon}_{xz} \cdot l_x$ $u_x^{NWB} = \bar{\varepsilon}_{xz} \cdot l_z, \quad u_x^{NWT} = \bar{\varepsilon}_{xz} \cdot l_z$

The following primary node displacements were imposed in each case:
$u_x^{SWB} = u_y^{SWB} = u_z^{SWB} = 0$, $u_x^{SWT} = u_z^{SWT} = 0$, $u_y^{SEB} = 0$, $u_y^{NWB} = 0$.

3.4. Material properties

We next discuss the material models used for the fired clay and mortar joints, based on the two governing failure mechanisms in masonry: block failure and joint failure.

Block failure is typically governed by tensile cracks. We discretely modeled these cracks using XFEM, with a linear elastic material behavior for the solid. The orthotropic material strength of extruded fired clay was accounted for by using the orthotropic Hoffman criterion (Hoffman, 1967) for crack initiation. The onset of a crack was controlled by the Virtual Crack Closure Technique (VCCT). Considering the findings of Bocca et al. (1989), Eis and Vassilev (2013), and Hannawald (2006), we chose the mode-I fracture energy as $G_{\mathrm{I,c}}^{\max} = 0.025\ \mathrm{J/mm^2}$. Following Kiefer et al. (2017), we defined the fracture energy for modes II and III as 20 times larger. In the framework of XFEM, cracks were allowed to form anywhere in the model, with one restriction: no crack was allowed to initiate within a radius of 20 mm from an existing crack tip. This was done to avoid the formation of multiple cracks in a small area, within the same loading step.

We used both transversally isotropic stiffness behavior (see Table 2) and transversally isotropic strengths (see Table 3), which is a good

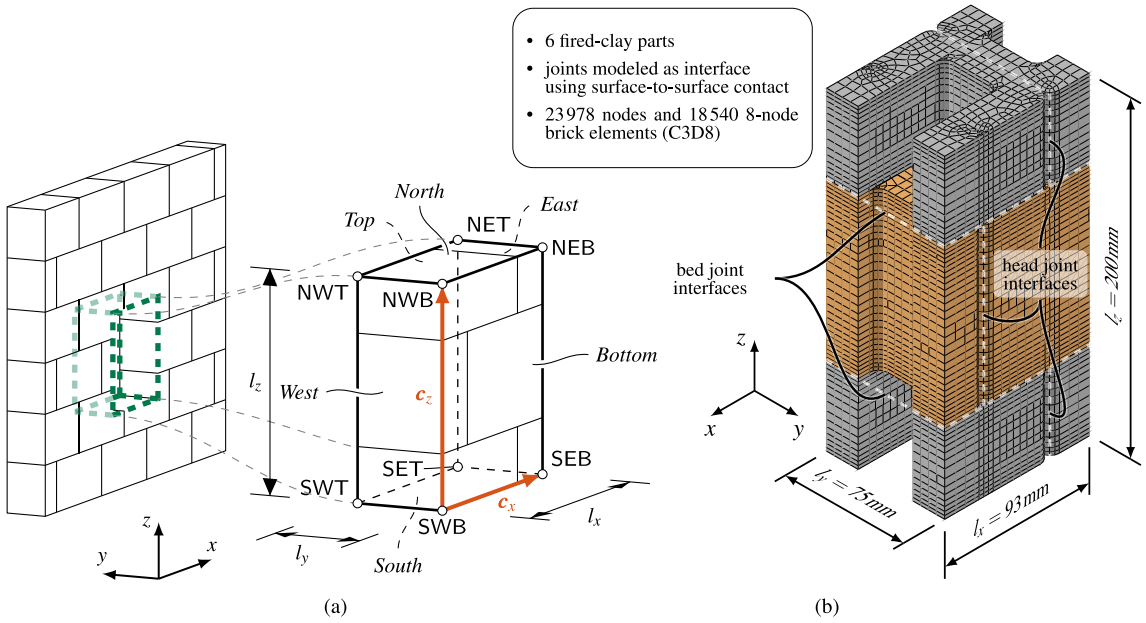

Fig. 6. Composition and geometry of the chosen repeating unit cell as part of the entire structure (a) and the FE model (b). The naming convention in (a) is based on the suggestions from Böhm (2023).

Table 2
Transversally isotropic stiffness parameters for fired clay.

Fired clay				
$E_{LL} = E_{ZZ}$	E_{TT}	$\nu_{TZ} = \nu_{LZ} = \nu_{LT}$	$G_{TZ} = G_{LT}$	G_{TZ}
13 500 MPa	8738 MPa	0.2	3500 MPa	5500 MPa

Table 3
Transversally isotropic strength parameters for fired clay in MPa.

Tension			Compression			Shear		
$\sigma_{t,L}$	$\sigma_{t,T}$	$\sigma_{t,Z}$	$\sigma_{c,L}$	$\sigma_{c,T}$	$\sigma_{c,Z}$	$\sigma_{s,TZ}$	$\sigma_{s,LZ}$	$\sigma_{s,LT}$
7.009	4.834	7.009	24.17	18.61	24.17	8.308	9.547	8.308

Table 4
Stiffness and damage properties for the mortar interface.

Interface stiffness		Damage properties		
K_{nn}	$K_{ss} = K_{tt}$	$\sigma_{f,\perp}$	$\tau_{m,ini}$	μ_m
5000 N/mm	2083 N/mm	0.3 MPa	1.4 MPa	0.3

Table 5
Head joint interface properties used for each joint type.

	HJM mortar	HJC contact	HJG gap
Cohesive behavior	✓	–	–
Friction	✓	✓	–
Interface damage	✓	–	–
Pressure-overclosure	✓	–	–

approximation of the orthotropic behavior of extruded fired clay according to Buchner et al. (2022). We derived the stiffness parameters and the material strengths from Kiefer et al. (2017) and Suda et al. (2021) considering this transversal isotropy. Thereby, the material direction follows the locally varying L-T-Z coordinate system shown in Fig. 5.

Joint failure manifests either in tensile or shear failure of the mortar, or tensile or shear failure of the interface (Van der Pluijm, 1999). Since we reduced the mortar joints to an interface with no thickness, both failure mechanisms were considered in one criterion. Thus, the weaker link (either the interface or the mortar itself) is relevant for failure. For modeling the interface behavior, we used cohesive behavior combined with a quadratic stress interaction criterion for identifying failure

$$\left(\frac{\langle\sigma_\perp\rangle}{\sigma_{f,\perp}}\right)^2 + \left(\frac{\tau}{\tau_{m,ini} - \mu_m \cdot \sigma_\perp}\right)^2 = 1, \tag{1}$$

with the stress component perpendicular to the joint $\sigma_\perp$, the shear stress τ, the tensile strength perpendicular to the joint $\sigma_{f,\perp}$, the initial value of the shear strength $\tau_{m,ini}$, and the friction coefficient μ_m. Note, that the stress component perpendicular to the joint is nested within Macauley brackets (i. e., $\langle\cdot\rangle$); thus, only tensile stresses are considered. Using cohesive behavior for interfaces in Abaqus results in a linear traction-separation law in tension, but a hard contact in compression (see the Abaqus documentation Dassault Systèmes, 2022). Since the mortar joints also show compressive deformations in reality, we used an additional tabular pressure-overclosure definition from Reismüller et al. (2023b). Using this definition, the coupled interfaces can overlap, while linearly building up pressure, accounting for the stiffness of the mortar. Additionally, we allowed for a small compressive stress at zero overclosure to overcome numerical instabilities at the beginning of the simulations.

The softening behavior of the joint was modeled exponentially on a displacement basis with a maximum displacement $u_{pl} = 0.15$ mm and an exponent $a = 5$ (for the equations refer to the Abaqus documentation Dassault Systèmes, 2022). We considered the mortar to be isotropic and used the material properties from a previous study (Reismüller et al., 2023b), where we derived the material properties by simulating shear tests on masonry triplets (see Table 4).

While we considered one type of bed joint, i. e., a 1 mm thick mortar layer, we wanted to compare three common types of head joints: a mortared head joint (HJM), frictional contact (HJC) in the head joint, and no contact in the head joint (HJG). For considering these three types, we altered the interface properties of the head joint. Table 5 shows the interface properties for each specific joint type.

3.5. Load application and sampling procedure

As discussed in Section 3.2, we can simulate arbitrary macroscopic in-plane *strain* states via imposing displacements at the primary nodes

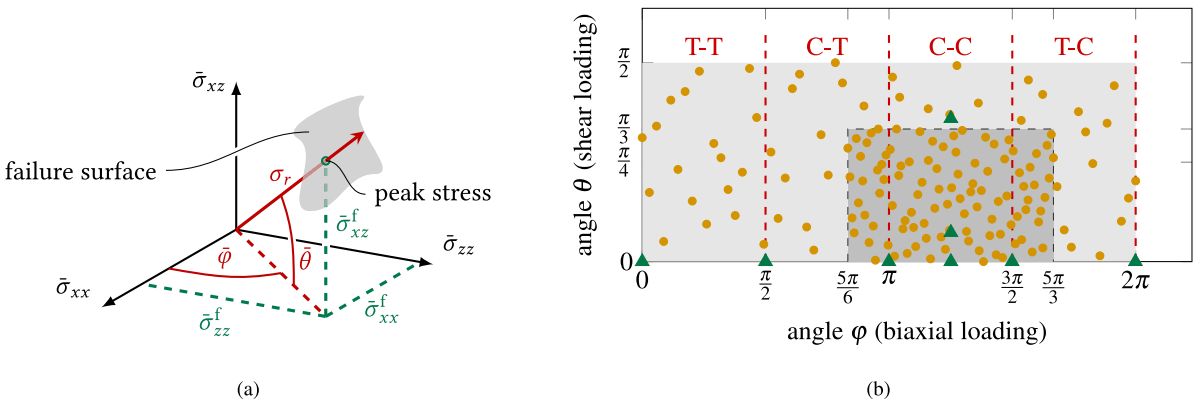

Fig. 7. (a) Spherical coordinates for the stress components and the intersection of the load path with the failure surface. (b) Example for loading combinations randomly sampled with LHS. The sample density in the darker area was chosen five times as large as in the lighter area. Red capital letters denote the loading regime (C . . . Compression, T . . . Tension). Each circle shows one sampled loading combination, the triangles mark the seven loading combinations proposed by Lourenço et al. (1996, 1997). (For interpretation of the references to color in this figure legend, the reader is referred to the web version of this article.)

of the repeating unit cell. However, for deriving a failure surface, we require macroscopic *stress* states. Thus, we used the unit cell concept to calculate the macroscopic stiffness tensor of the repeating unit cell (Anthoine, 1995) and derived the macroscopic strains from the macroscopic stresses via Hooke's law.

For numerically deriving a failure surface, a representative set of loading states needs to be considered. This failure surface characterizes the material failure due to interacting axial stresses $\bar{\sigma}_{xx}$ and $\bar{\sigma}_{zz}$ and the shear stress $\bar{\sigma}_{xz}$. Expressing this loading state in spherical coordinates, by two angles, $\bar{\varphi}$ and $\bar{\theta}$, and the stress resultant $\bar{\sigma}_r$ (see Fig. 7(a)), the load level can be easily controlled for a fixed loading direction. The stresses can be transformed into cartesian coordinates in the following way:

$$\bar{\sigma}_{xx} = \bar{\sigma}_r \cdot \cos\bar{\varphi} \cdot \cos\bar{\theta}, \tag{2}$$

$$\bar{\sigma}_{zz} = \bar{\sigma}_r \cdot \sin\bar{\varphi} \cdot \cos\bar{\theta} \text{ and} \tag{3}$$

$$\bar{\sigma}_{xz} = \bar{\sigma}_r \cdot \sin\bar{\theta}. \tag{4}$$

The three variables $\bar{\varphi}$, $\bar{\theta}$, and $\bar{\sigma}_r$ define the sampling domain for deriving the failure surface. By an adaptive load incrementation in the FE simulation, a given orientation ($\bar{\varphi}$, $\bar{\theta}$) is assessed for material failure for all stress resultants. Therefore, we considered only the two angles in the sampling procedure.

The next step was to define a sampling range. While reasonable values for $\bar{\varphi}$ reach from 0 to 2π, $\bar{\theta}$ was sampled from 0 to $\pi/2$, describing a hemisphere. To ensure an even distribution of the samples over this domain, LHS (McKay et al., 1979) was used for choosing a reasonable set of loading paths. For n samples, the sample domain is evenly divided into n columns and n rows. The samples are randomly placed inside this domain, such that there is exactly one sample in each column and row, leading to a set of samples, which is evenly distributed over the given domain.

Considering the failure surfaces found by Ganz (1985) and Lourenço et al. (1996, 1997), the compressive strengths are expected to be significantly larger than the tensile strengths. This implies that the failure surface is further from the coordinate origin in the compressive loading regime. Since the LHS creates samples evenly distributed over the given domain, the distance between the calculated points on the surface is larger in the compressive than in the tensile loading regime. Therefore, the sample density in the compressive loading regime was chosen five times as large as in the tensile loading regime (see Fig. 7(b)).

With a stress resultant of $r = 15$ MPa (large enough to cause material failure for any combination of $\bar{\varphi}$ and $\bar{\theta}$), we randomly generated 150 samples for each head joint type, resulting in 450 simulations (see also Fig. 8). Additionally, we added the seven loading states proposed by Lourenço et al. (1996, 1997), which are marked by green triangles in Fig. 7(b).

3.6. Computational aspects

The simulations were performed on a high-performance computing cluster with 168 CPUs in total. Using eight CPU cores in parallel, one simulation took approximately 144 min on average to finish. For overcoming numerical instabilities related to the initiation of contact between two surfaces, an additional step was introduced at the beginning of the calculation. In this step, the displacements of each primary node were set to zero. Due to the chosen pressure-overclosure formulation with an insignificant compressive contact stress at zero distance between the surfaces, contact could be ensured in each relevant point, before the displacement-controlled loading was applied in the following step. To prevent numerical instabilities when solving the interface damage conditions, damage stabilization was used for the cohesive interfaces.

3.7. Postprocessing

After the simulations were completed, we extracted the results by using the postprocessing procedure described in the following sections (see Fig. 8). Two different results were most interesting to us: the effective stresses and strains on the macroscopic level, which are essential for defining a macroscopic failure surface, and the failure mechanism on the mesoscopic scale, which gives insights into the overall behavior and helps define the exact point of failure.

At first, we derived the macroscopic stresses and strains by homogenizing the stresses and strains on the mesoscopic scale over the repeating unit cell. Afterward, we used the macroscopic stress–strain relation and indicators on the mesoscopic scale to specify a failure point. These procedures are discussed next.

3.7.1. Obtaining macroscopic stresses and strains

For homogenizing the behavior from the mesoscopic to the macroscopic scale, we assume that the behavior of the smallest possible repeating unit cell in the wall is representative for each point in the homogenized macroscopic wall. The unit cell concept is well suited for meso-to-macro homogenization since the displacements and reaction forces of the total structure are concentrated in the primary nodes of the unit cell. Thus, the stresses and strains can be easily calculated from the extracted reaction forces RF_i and displacements u_i by considering the dimensions l_i of the repeating unit cell as follows:

$$\bar{\sigma}_{xx} = \frac{RF_{xx}}{l_y \cdot l_z}, \quad \bar{\sigma}_{zz} = \frac{RF_{zz}}{l_x \cdot l_y}, \text{ and } \bar{\sigma}_{xz} = \frac{1}{2} \cdot \left(\frac{RF_{xz}}{l_y \cdot l_z} + \frac{RF_{zx}}{l_y \cdot l_z} \right) \text{ as well as} \tag{5}$$

$$\bar{\varepsilon}_{xx} = \frac{u_{xx}}{l_x}, \quad \bar{\varepsilon}_{zz} = \frac{u_{zz}}{l_z}, \text{ and } \bar{\varepsilon}_{xz} = \frac{1}{2} \cdot \left(\frac{u_{xz}}{l_x} + \frac{u_{zx}}{l_z} \right). \tag{6}$$

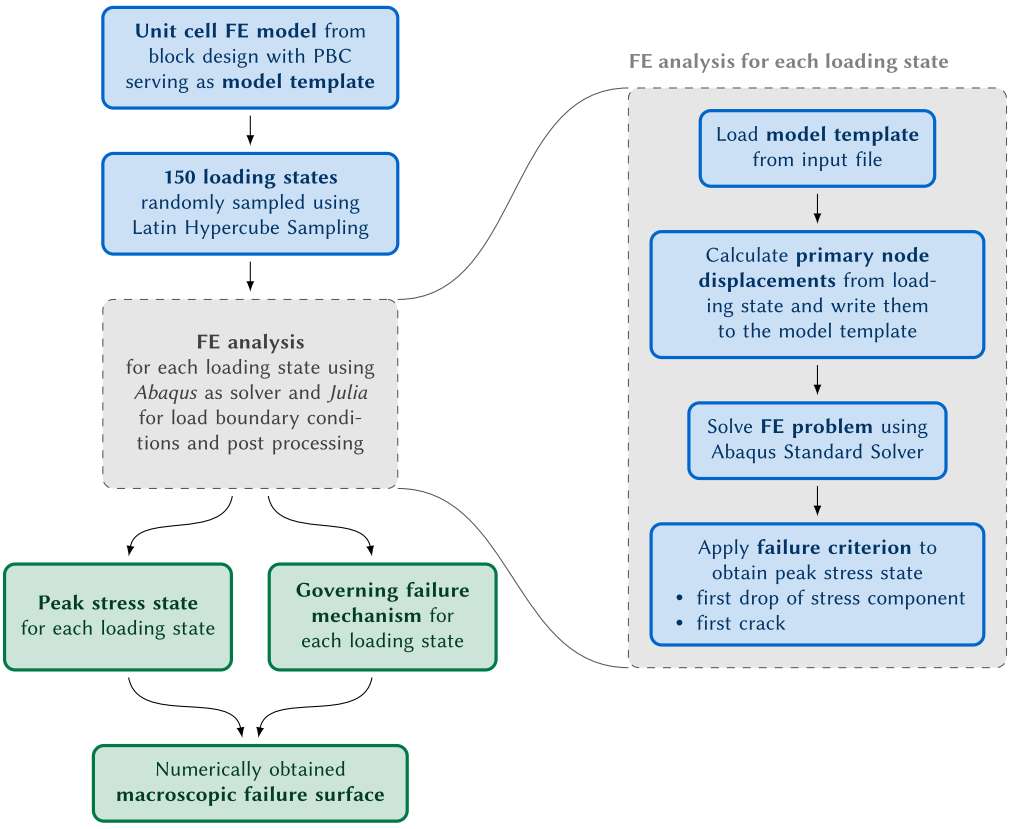

Fig. 8. Overview of the simulation procedure.

3.7.2. Detecting failure

For defining the macroscopic failure stress state for each simulation we considered the same two-part failure criterion as we used in Reismüller et al. (2023b). At the macroscopic scale, the largest stress before the first significant decrease of a stress component was considered the peak stress. This criterion was relevant, especially for joint failure, which occurs much more ductile than block failure. Furthermore, a second criterion considering the first crack within the blocks was defined to capture block failure. This was necessary, since some of the simulations, where block failure was relevant, did not produce a significant drop in stresses. Instead, these simulations aborted when the first crack opened. Considering the findings of Kiefer et al. (2017) and Suda et al. (2021), this is a good approximation, since there, the first crack also occurred just before the peak stress was reached.

4. Results and discussion

In the following section, the simulation results are presented and discussed. First, failure mechanisms are identified from the results of the simulations with the simplified geometry. Then, the Rankine–Hill surface (Lourenço, 1996; Lourenço et al., 1997) and the failure surface of Ganz (1985) are calibrated using the simulation results and compared to the numerically obtained failure surface. Next, the developed procedure for defining a failure surface is applied to two real block designs and the results are discussed. Finally, the obtained results are gathered, to propose a concept for calibrating the Rankine–Hill surface, taking the differences between the numerically-obtained failure surfaces and the Rankine–Hill surface into account. For the sake of brevity, only the model with mortared head joints is discussed in detail, while the results for the other two models are presented in the supplementary material.

4.1. Numerically obtained failure surface

Fig. 9 shows the numerically obtained failure surface for the model with mortared head joints. Each point in Fig. 9a represents the peak stress state of one simulation. The filled areas in the background mark regions, where we observed similar failure mechanisms in the simulations. In the following, we will discuss the peak stresses starting with the tensile regime and then moving clockwise around the boundary of the failure surface.

In the tensile regime, the maximum vertical macroscopic peak stress was 1.303 MPa, while the maximum horizontal macroscopic peak stress was 0.818 MPa. On the right side of the failure surface, the horizontal macroscopic peak stress stayed constant with increasing vertical compression until the vertical stress reached −9.157 MPa, which was the maximum vertical compressive peak stress observed in the simulations. On the bottom side, this maximum vertical compressive peak stress stayed constant with increasing horizontal compression until the horizontal stress reached −9.023 MPa. On the left side, the failure surface showed a parabolic shape with a maximum horizontal compressive peak stress of −10.325 MPa. The top side of the failure surface showed a linear relationship between the horizontal and the vertical macroscopic stress, with an increasing vertical macroscopic peak stress for decreasing horizontal compression. The macroscopic peak shear stress was 3.928 MPa occurring at $\bar{\sigma}_{xx} = -4.992$ MPa and $\bar{\sigma}_{zz} = -5.286$ MPa.

Vertically perforated clay block masonry is known to show significant strength anisotropies. Typically, the ratio of the macroscopic peak stress parallel to the bed joints to the macroscopic peak stress perpendicular to the bed joints is between 0.25 and 0.63, depending on the block design (Lourenço, 1996; Lourenço et al., 1997). However, the maximum horizontal macroscopic peak stress in the simulations was similar to the maximum vertical macroscopic peak

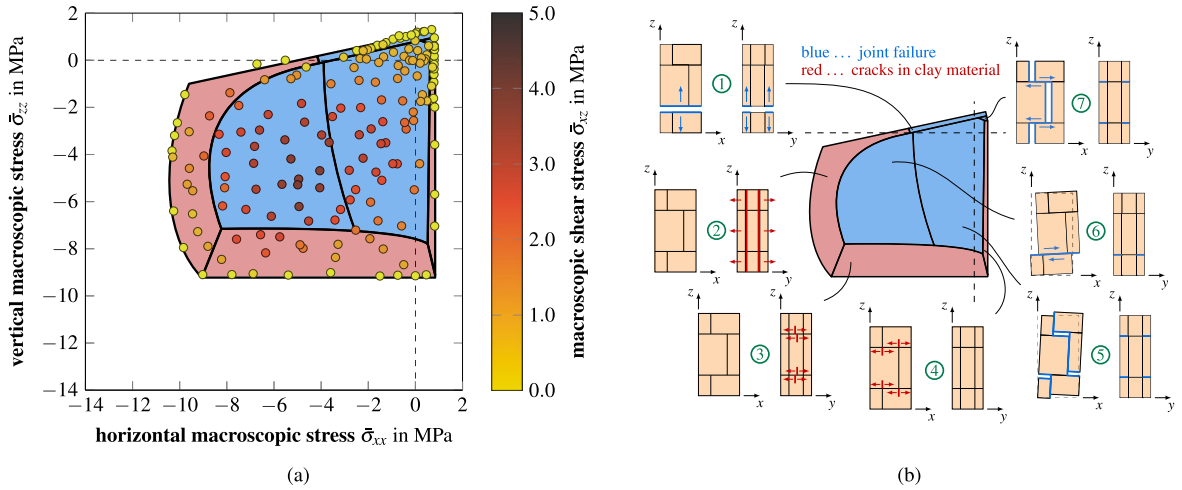

Fig. 9. Numerically obtained failure surface for the model with mortared head joints (HJM). Each point in (a) represents the peak stress state of one simulation. The filled areas in (b) mark regions with similar failure mechanisms. (For interpretation of the references to color in this figure legend, the reader is referred to the web version of this article.)

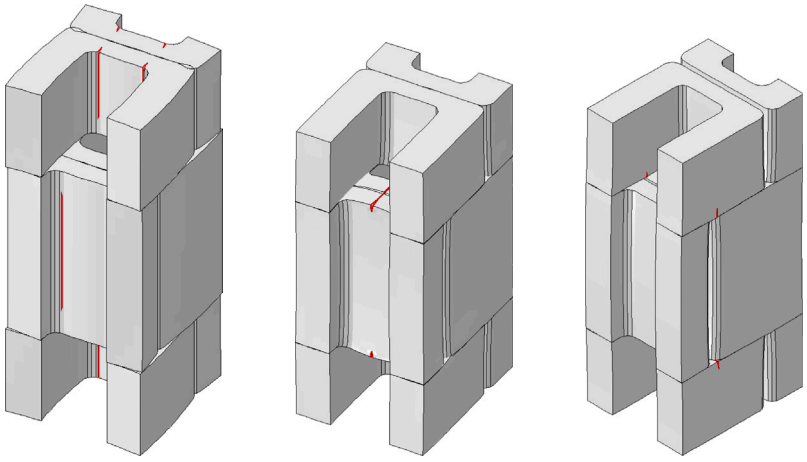

Fig. 10. Block failure mechanisms observed in the simulations.

stress, which most likely roots in the given block design. Comparable block designs, such as typical hollow concrete block masonry, tend to show a less pronounced strength anisotropy (see, e. g., Lourenço et al. (1996, 1997)). Nevertheless, the simulations did show a significant anisotropy considering the failure mechanisms, which we will discuss in the following.

The observed failure mechanisms, labeled 1 to 7, are assigned to the filled areas in Fig. 9b. Note, that the failure mechanisms are not necessarily unique to the corresponding area, but are the dominating ones. While surfaces, where block failure was observed, are filled red (2, 3, and 4), surfaces, where joint failure was observed, are filled blue (1, 5, 6, and 7).

Failure mechanism 1 was observed under governing vertical tensile stresses and is characterized by tensile failure of the bed joints since the vertical tensile stresses introduce tensile stresses in the bed joints. With increasing horizontal compression, shear stresses are additionally introduced in the bed joints, which leads to a decreasing vertical tensile strength of the bed joints (see Eq. (1)).

Failure mechanism 2 was observed under governing horizontal compression and is characterized by tensile cracks in the connection between transversal and longitudinal webs (see Fig. 10(a)). In a previous numerical study (Reismüller et al., 2023b), we traced back these cracks to bending moments, introduced to the transversal webs by deformation differences in the mortar head joints.

Failure mechanism 3 was observed under governing vertical compression and is characterized by tensile cracks in the transversal webs (see Fig. 10(b)) since large vertical compressive stresses lead to tensile stresses in the transversal web (see Kiefer et al. (2017), Suda et al. (2021), and Reismüller et al. (2023b)).

Failure mechanism 4 was observed under horizontal tension in combination with vertical compression and is characterized by tensile cracks in the longitudinal webs (see Fig. 10(c)). With decreasing vertical compression, the shear strength of the bed joints decreases (see Eq. (1)), which leads to a change to failure mechanism 7. When the shear strength of the bed joints falls below a certain value, joint failure occurs before the failure of the longitudinal webs.

Failure mechanism 5 was observed under governing shear stresses in combination with low horizontal compression and is characterized by a stepped shear failure of the bed joints and head joints. The inhomogeneous nature of masonry leads to a rotation of the blocks under shear loading (Mojsilović, 1995), introducing bending moments in the joints. In addition to the shear stresses parallel to the joints, these bending moments induce stresses perpendicular to the joints. Depending on the magnitude of the vertical and horizontal macroscopic stresses, tensile stresses perpendicular to the joints can occur. Thus, despite failure mechanism 5 being labeled as shear failure, especially with low vertical compression, a combination of shear and tensile failure was observed.

In contrast to the previous mechanism, failure mechanism 6, which was observed under governing shear stresses in combination with large horizontal compression, is characterized by a shear failure solely of the bed joints. This is because the larger horizontal compression leads to a larger shear strength of the head joints, which prevents joint failure there.

Failure mechanism 7 was observed in the tensile regime under governing horizontal tension and is characterized by tensile failure of the head joints and shear failure in the bed joints. This is because the horizontal tensile stresses introduce tensile stresses in the head joints and shear stresses in the bed joints. As discussed for failure mechanism 4, the shear strength of the bed joints increases with increasing vertical compression. Thus, increasing vertical compression leads to a change in failure mechanism from joint failure (7) to block failure (4).

Fig. 11 shows the peak stresses and failure mechanisms of the models with and without frictional contact in the head joints. Most of the previously described failure mechanisms were also observed in these models. However, some noteworthy differences compared to the model with mortar head joints occurred.

Despite showing similar maximum values for the tensile, compressive, and shear stresses, the failure surface of the model with frictional contact in the head joints (HJC) shows some differences in the overall shape, compared to the model with mortar head joints (Fig. 11a). Most notably, the maximum vertical compressive peak stress decreases with increasing horizontal compression (bottom side of the failure surface). Additionally, the maximum shear stress is reached at higher horizontal and vertical compressive stresses, although showing a similar magnitude. Thus, when moving along the hydrostatic axis in the compressive regime, the increase of the peak shear stress is less steep in the model with frictional contact in the head joints.

The failure surface of the model without contact in the head joints (HJG, Fig. 11b) shows a significantly different shape compared to both other models. Most notably, failure region 2, which is governed by block failure under horizontal compression, nearly vanished. Instead, under horizontal compression, failure is mainly governed by a shear failure of the bed joints, similar to failure mechanism 7 but in the opposite direction (region 8). This is because the horizontal compressive stresses are being transferred via shear stresses in the bed joints since no contact in the head joints is present. With the adapted interface condition in the joint interfaces, the horizontal compressive peak stress increases with increasing vertical compression in region 8. Hence, the maximum horizontal compressive peak stress is only 3.0 MPa, which is significantly lower than in the other models. Additionally, the maximum shear stress 2.5 MPa is 50% lower. While the maximum tensile peak stresses and the maximum vertical peak stress are similar to the other models, another noteworthy difference is the increasing vertical compressive peak stress with increasing horizontal compression in region 3.

4.2. Comparison to available failure surfaces

In the following, the numerically obtained failure surface of the model with mortar head joints (HJM) is compared to the failure surfaces of Ganz (1985) and Lourenço et al. (1996, 1997). A similar comparison for the models with frictional contact in the head joints and without any contact in the head joints is given in the supplementary material.

4.2.1. Failure surface according to Ganz

The failure surface of Ganz (1985) was calibrated to the simulations by adjusting the ten parameters of the failure criteria (see Appendix A) as follows: We obtained the uniaxial compressive masonry strengths $f_{m,x}$ and $f_{m,z}$, the vertical uniaxial tensile strength $f_{t,z}$, and the ratio of the horizontal tensile masonry strength to its compressive counterpart, ω_m, from the simulation results. The distance of the head joints, a_S, and the distance of the bed joints, a_L, are defined by the model's geometry. The remaining parameters, the cohesion shear stress c, the friction angle of the joints, φ, and the additional parameter μ, were calibrated to the simulations by minimizing the mean squared error between the numerically obtained peak stresses and the failure surface. The resulting failure surface and the chosen values for the parameters are shown in Fig. 12(a). The mean absolute error (MAE) between the numerically obtained peak stresses and the calibrated failure surface is 0.708 MPa.

The most noticeable difference between the numerically obtained peak stresses and the calibrated failure surface can be found under horizontal tension in combination with vertical compression (right side of the failure surface). Here, the failure surface predicts a decreasing horizontal tensile peak stress with increasing vertical compression, while staying constant in the simulations. Regarding the shear behavior, the calibrated failure surface predicts a 23% larger maximum shear stress than the simulations. Additionally, this peak occurs at a lower horizontal compression than in the simulations, leading to significant shear stress deviations in this region compared to the simulations.

4.2.2. Rankine–Hill failure surface

Next, we will compare the numerically obtained results to the Rankine–Hill surface (Lourenço, 1996; Lourenço et al., 1997). We calibrated the seven parameters of the Rankine–Hill surface in two different ways: (i) By determining the parameters from the seven simulations of ideal loading states and (ii) by minimizing the mean squared error between the numerically obtained peak stresses and the failure surface ("Opt").

First, we derived the parameters by simulating the seven loading combinations proposed by Lourenço et al. (1996, 1997) (see Fig. 4). The resulting failure surface and the chosen values for the parameters are shown in Fig. 12(b). Therein, the seven simulations used for the calibration are marked with squares.

Using the seven suggested loading combinations results in significant differences between the Rankine–Hill surface and the numerically obtained peak stresses, which is reflected by a large MAE of 2.395 MPa. The Rankine–Hill surface predicts a 49.8% higher maximum vertical compressive stress and a 46.5% lower maximum horizontal compressive stress than the simulations. Given that only seven loading states were considered, the Rankine-type criterion shows good agreement with the simulations, and the maximum shear stress has a similar magnitude, as the numerically obtained results.

In the second step, we optimized the parameters of the Rankine–Hill surface by minimizing the mean squared error between the numerically obtained peak stresses and the failure surface. While Lourenço et al. suggests the seven loading combinations as a good option for minimizing the effort and maximizing the accuracy of the calibration, he also states that the mean error optimization is better, if enough data is available. The resulting failure surface and the chosen values for the parameters are shown in Fig. 13. The MAE between the numerically obtained peak stresses and the calibrated failure surface is 0.832 MPa. The mean error optimization delivers a significantly better fit than calibration with the seven loading combinations. However, the Rankine–Hill surface still shows differences compared to the numerically obtained peak stresses. The vertical uniaxial compressive strength is predicted to be 21.0% lower than in the simulations and the vertical uniaxial tensile strength is predicted to be 62.5% lower, whereas the horizontal uniaxial compressive strength is predicted to be 37.3% higher. Additionally, some simulations with large horizontal compressive stresses are not captured by the failure surface. Furthermore, the peak shear stress is predicted to be 17.0% lower than in the simulations.

The most noticeable differences can be found under vertical tension in combination with horizontal compression (top part of the failure surface) and under large vertical compression in combination with horizontal compression (bottom side of the failure surface), where the calibrated Rankine–Hill surface predicts significantly smaller peak stresses than the simulations. In general, the linearly decreasing vertical

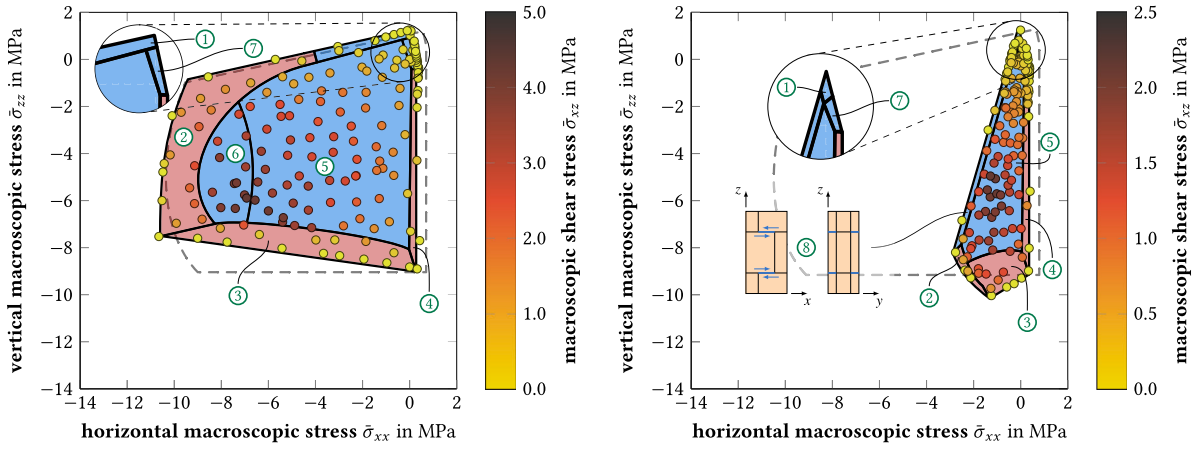

Fig. 11. Numerically obtained failure surface for (a) the model with frictional contact in the head joints (HJC) and (b) the model without any contact in the head joints (HJG). Each point represents the peak stress state of one simulation. The filled areas mark regions with similar failure mechanisms. The numbers refer to the failure mechanisms in Fig. 9b.

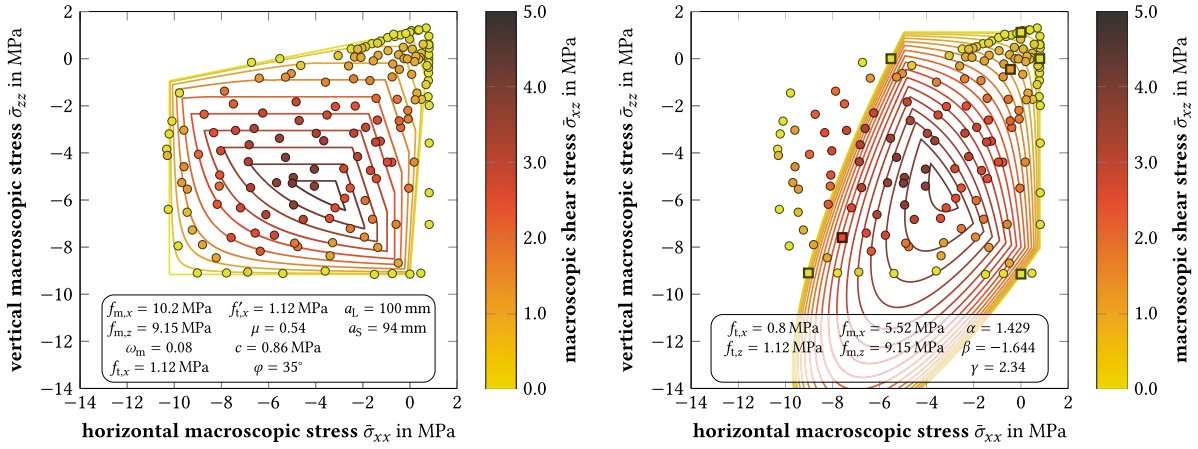

Fig. 12. Calibrated failure surfaces using the numerically-obtained peak stresses from the simplified model with mortared head joint: (a) failure surface after Ganz (1985) and (b) Rankine–Hill surface after Lourenço et al. (1996, 1997). The seven peak stress states used for calibrating the Rankine–Hill surface are marked with squares.

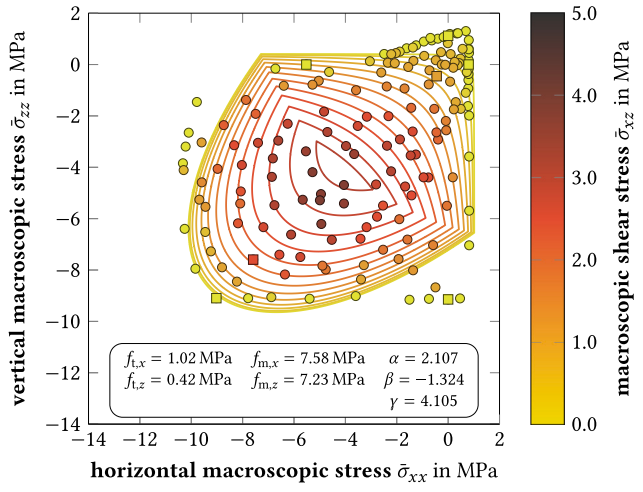

Fig. 13. Calibrated Rankine–Hill surface for the simplified model with mortared head joints using mean squared error optimization (Opt). The seven peak stress states used for calibrating the Rankine–Hill surface in Fig. 12(b) are marked with squares.

tensile peak stress with increasing horizontal compression (top part of the simulated peak stresses, Failure Mechanism 1) cannot be replicated by the Rankine–Hill surface, since it predicts a constant vertical tensile peak stress. Furthermore, the Rankine–Hill surface is smooth in the compressive regime, while the simulation results show a distinct edge, where the failure mechanism changes from horizontal compressive block failure (Region 2) to vertical compressive block failure (Region 3).

Removing the simulations where failure mechanisms 1 and 3 were governing from the set of peak stress states and applying the mean squared error optimization leads to the failure surface shown in Fig. 14. The obtained Rankine–Hill surface shows good agreement with the simulations and the vertical uniaxial compressive and tensile peak stresses are predicted similarly to the simulations, while the maximum shear stress is predicted to be 21% lower than in the simulations. The MAE between the numerically obtained peak stresses and the calibrated Rankine–Hill surface is 0.867 MPa, which is only 4.2% larger than the MAE using all the simulations. This shows that the Rankine–Hill surface can capture the majority of the simulations. However, we could identify some regions, where the simulations show a qualitatively different behavior than the Rankine–Hill surface, suggesting a more complex failure envelope of vertically perforated clay block masonry

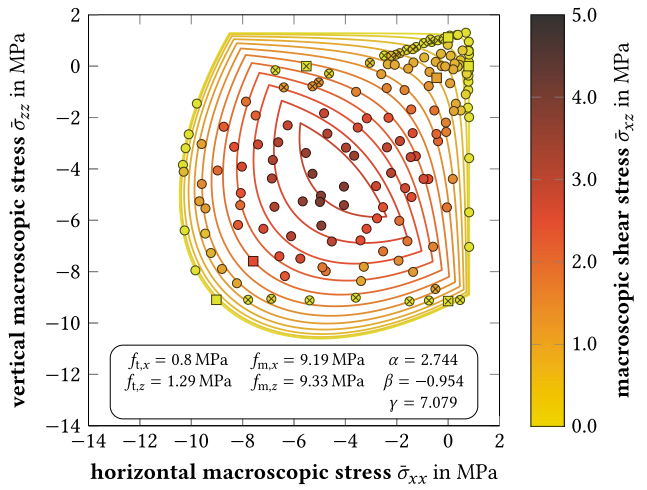

Fig. 14. Calibrated Rankine–Hill surface for the simplified model with mortared head joints using mean squared error optimization (Opt) without the simulations where Failure Mechanisms 1 and 3 were governing. The seven peak stress states used for calibrating the Rankine–Hill surface in Fig. 12(b) are marked with squares.

than the Rankine–Hill surface can provide. While the differences in failure region 1 can also be seen, when Lourenço et al. (1996, 1997) fitted the Rankine–Hill surface to the experimental data from Page (1983), the differences under large vertical compression are most likely a phenomenon of vertically perforated clay block masonry, since the change in failure mechanism leading to this difference is caused by the perforations.

In conclusion, the mean squared error optimization on all peak stress states leads to a good representation of the results, assuming that the numerically obtained peak stresses resemble the real behavior of vertically perforated clay block masonry. However, the optimization procedure also leads to a significant underestimation of the vertical compressive peak stress and the vertical tensile peak stress. Adapting the set of peak stress state showed that the Rankine–Hill surface can capture the majority of the simulations, while still showing some discrepancies. Thus, a slightly more complex failure surface is needed to fully utilize the strength of the masonry. Although the failure surface from Ganz shows a better agreement with the simulations, the Rankine–Hill surface will be used for the following discussion, since it is better suited for use within finite element software.

4.3. Application to real block designs

To further verify our model, we used the developed procedure to calibrate the Rankine–Hill surface for two different real block designs, the SwissModul 15 (Zürcher Ziegeleien, 2023) used in the experiments from Bitterli and Salmanpour (2014, 2017), and an insulation-filled block from Wienerberger (2023).

The SwissModul 15 is a vertically perforated clay block with a height of 190 mm, a length of 290 mm, and a width of 150 mm. The blocks are used in conjunction with 10 mm thick mortar bed joints and mortar-filled head joints with similar thickness. For calibrating the failure surfaces, we used the 34 simulations from our previously published study (Reismüller et al., 2023b). In that study, we used the numerical unit cell model to simulate the experiments from Bitterli and Salmanpour (2014, 2017).

Simulating the loading states suggested by Lourenço et al. (1996, 1997), we obtained the failure surface shown in Fig. 15(a) with an MAE of 0.868 MPa. Using the mean squared error optimization procedure, we obtained the failure surface shown in Fig. 15(b). The obtained Rankine–Hill surface is in good agreement with the simulations. However, a similar discrepancy between the surface and the numerically obtained peak stresses can be found under vertical compression, when failure mechanism 3 is relevant. In this region, the calibrated Rankine–Hill surface predicts up to 9.2% larger peak stresses than obtained in the simulations. Considering the second region with discrepancies identified with the simplified model (i. e., where Failure Mechanism 1 was governing), we cannot make a statement for this block design, since we did not simulate enough loading combinations in this region. The MAE of the Rankine–Hill surface calibrated for the SwissModul 15 is 0.417 MPa using all simulations. Thus, the optimization procedure leads to a better, yet more conservative fit of the Rankine–Hill surface with the numerically obtained peak stresses.

The second block design we used for calibrating the Rankine–Hill surface is an insulation-filled block from Wienerberger (2023), which is 248 mm long, 249 mm high, and 365 mm wide. It is typically used in conjunction with 1 mm thin bed mortar joints and dry head joints. Thus, frictional contact was used in the head joints in the simulations. We calibrated the Rankine–Hill surface shown in Fig. 16 to 31 simulations. The model was created using the same modeling strategies as used for the previous simulations.

Notably, the results of the simulations predict a much more anisotropic behavior than with the SwissModul 15 and the simplified block design with a ratio of the horizontal compressive peak stress to the vertical compressive peak stress of 0.35. This is also reflected in the calibrated Rankine–Hill surface, which is in good agreement with the simulations. Using the loading states suggested by Lourenço et al. (1996, 1997), we obtained the failure surface shown in Fig. 16(a) with an MAE of 0.446 MPa. The failure surface obtained with the optimization procedure is presented in Fig. 16(b). With this geometry, the optimized Rankine–Hill surface predicts up to 4.2% smaller peak stresses than obtained in the simulations in the region, where failure mechanism 3 is relevant. Additionally, we observed a similar discrepancy under vertical tension combined with horizontal compression, as identified with the simplified model. The MAE of the calibrated Rankine–Hill surface is 0.372 MPa using all simulation. Similar to the SwissModul 15, the optimization procedure yielded a better, yet slightly more conservative fit of the Rankine–Hill surface.

4.4. Concept for deriving a numerically calibrated failure surface

Considering all the results presented in the previous sections, we propose the following concept for deriving a numerically calibrated failure surface for masonry. Since the Rankine–Hill surface depicts the numerically obtained peak stresses very well in most regions and can easily be implemented into FE software, we recommend using it for macroscopic simulations of vertically perforated clay block masonry. Simulating the loading states proposed by Lourenço et al. (1996, 1997) for the calibration of the Rankine type surface (i. e. parameters $f_{t,x}$, $f_{t,z}$, and f_{α}) led to a good agreement with the numerically obtained peak stresses in each case. Hence, we suggest using these three simulations for the calibration of this part of the surface (see Fig. 17). However, using the suggested loading states for the calibration of the Hill type surface (i. e. parameters $f_{m,x}$, $f_{m,z}$, f_{β}, and f_{γ}) did not always lead to a good agreement with the numerically obtained peak stresses. While we obtained good agreement for the real block geometries, we observed significant deviations for the simplified block design. Thus, we suggest simulating seven additional loading states for the calibration of the Hill-type surface (see Fig. 17b). We chose these such that the loading path is directed towards the regions, where we observed the largest discrepancies between the numerically obtained peak stresses and the calibrated Hill-type surface. Using these additional peak stresses, we can derive the parameters for the Hill-type surface using a mean error optimization procedure. Therefore, the resulting failure surface will underestimate some of the peak stresses in failure region 2, but also show fewer differences to the simulations in failure region 3.

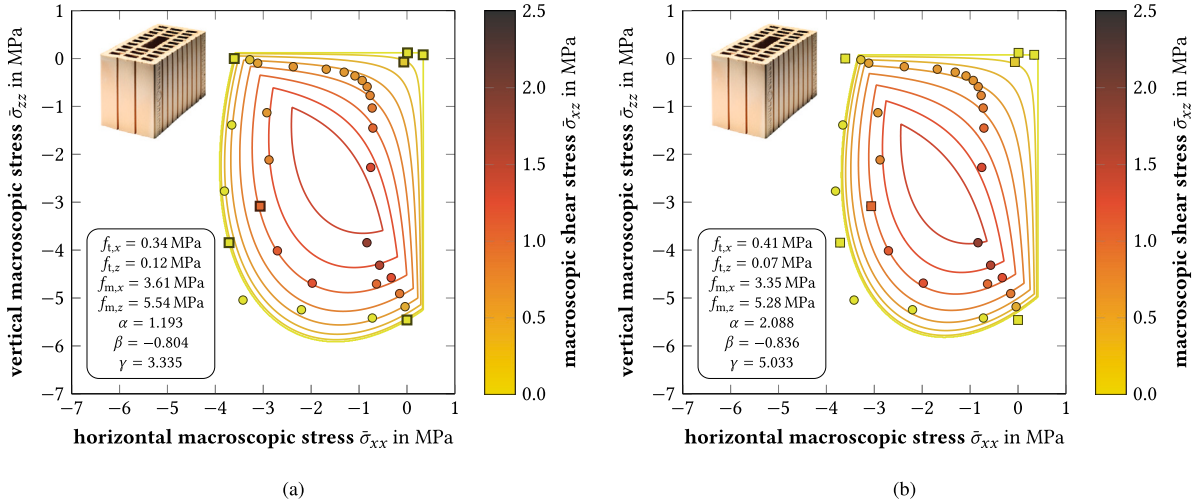

Fig. 15. Calibrated Rankine–Hill surfaces for SwissModul 15 with mortared head joints: (a) was calibrated using the loading states suggested by Lourenço et al. (1996, 1997) and (b) was calibrated using the mean squared error optimization procedure. The seven peak stress states used for calibrating the Rankine–Hill surface in (a) are marked with squares.

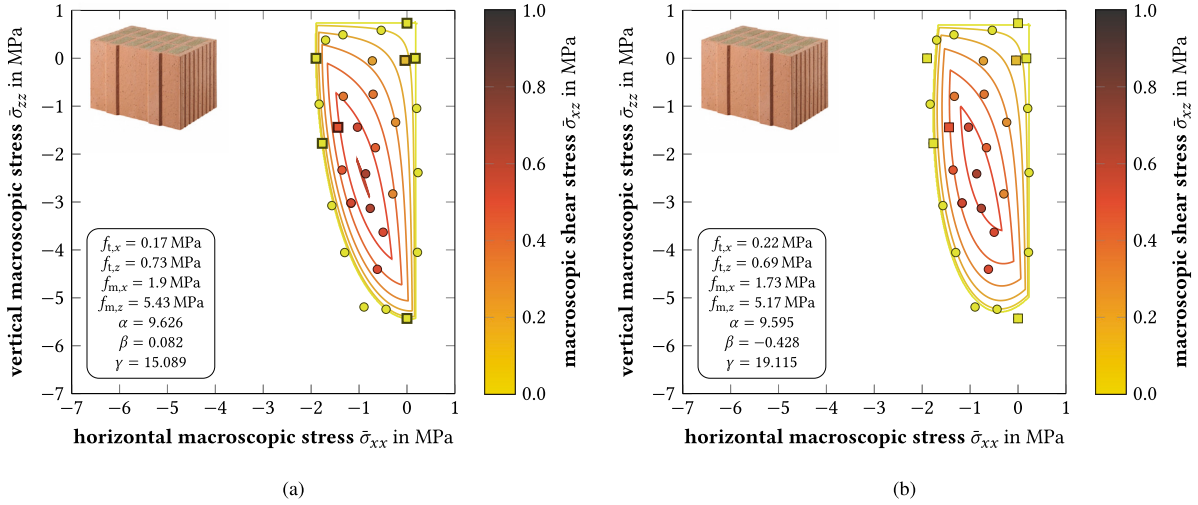

Fig. 16. Calibrated Rankine–Hill surfaces for the Wienerberger block with contact in the head joints: (a) was calibrated using the loading states suggested by Lourenço et al. (1996, 1997) and (b) was calibrated using the mean squared error optimization procedure. The seven peak stress states used for calibrating the Rankine–Hill surface in (a) are marked with squares.

5. Conclusion and outlook

Within this work, we presented a new approach to develop failure surfaces for vertically perforated clay block masonry under in-plane loading using numerical simulations. Using a previously published unit cell FE model (Kiefer et al., 2017; Reismüller et al., 2023b) and a simplified block design, we derived the peak stresses from 450 simulations in total, with 150 arbitrarily generated loading states. Additionally, we investigated the influence of the head joint, by considering three different types, i. e., a mortared head joint, frictional contact in the head joint, and no contact in the head joint. Hence, we were able to numerically derive failure surfaces for the three different head joint types. For each type, we also identified seven different realistic failure mechanisms and assigned these mechanisms to regions of the failure surface.

After the rigorous discussion of the numerically-obtained failure surfaces, we compared them to the failure surfaces proposed by Ganz (1985) and Lourenço et al. (1996, 1997), by calibrating the necessary parameters to the simulation results. The failure surface of Ganz was found to be in good agreement with the numerically-obtained failure surfaces, with the most significant difference under horizontal tension. Additionally, the maximum shear stress was found to be 23% higher than in the numerically-obtained failure surface. The quality of the fit of the failure surface after Lourenço et al. depends on the chosen calibration procedure. While calibrating the failure surface by simulating the seven loading combinations suggested by Lourenço et al. (1996, 1997) resulted in a poor agreement with the numerically-obtained peak stresses, a mean squared error optimization procedure yielded a good agreement. Thereby, two regions with significant differences were identified, i. e., the region of vertical tension and the region of vertical compression.

To assess this difference in more detail, we used the developed procedure to calibrate the Rankine–Hill surface for two real block designs. The results showed, that the differences also occur for real block designs, although the differences are less significant. Nevertheless, the Rankine–Hill surface overestimated the peak stress of the numerical model up to 12.8%, suggesting a more complex failure surface.

Finally, we proposed a concept to numerically calibrate the parameters of the Rankine–Hill surface, taking the differences between the numerically-obtained failure surfaces and the Rankine–Hill surface into account. Therefore, we suggested simulating the seven loading combinations proposed by Lourenço et al. (1996, 1997) for calibrating

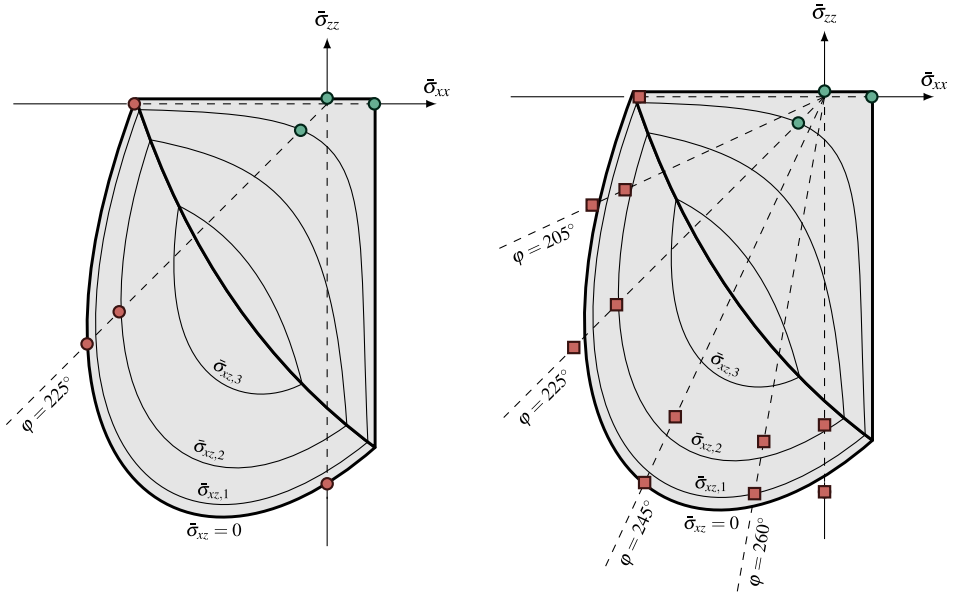

	$\bar{\varphi}$	$\bar{\theta}$	
Rankine	0°	0°	a
	0°	90°	a
	225°	13.2°	a
Hill	180°	0°	a
	205°	0°	
	205°	64.5°	
	225°	0°	a
	225°	64.5°	a
	245°	0°	
	245°	64.5°	
	260°	0°	
	260°	64.5°	
	270°	0°	a
	270°	64.5°	

[a] Suggested by Lourenço [15].

Fig. 17. Concept for deriving a numerically calibrated Rankine–Hill surface. (a) Calibration with the loading states suggested by Lourenço et al. (1996, 1997), and (b) mean error optimization of $f_{m,x}$, $f_{m,z}$, β, and γ using 11 simulations. Peak stresses used for calibration of the Rankine-type surface are filled green, and those used for calibration of the Hill-type surface are filled red. Simulations used for mean error optimization are marked with squares. (For interpretation of the references to color in this figure legend, the reader is referred to the web version of this article.)

the surface, and to simulate two additional loading combinations with governing vertical compressive stresses to assess the quality of the fit and to adjust the parameters accordingly.

In future research, we could improve the proposed concept by considering the following aspects: Since the model is restricted to in-plane loading, the next step would be to extend the model to out-of-plane loading, like Mojsilović (1995) did for the failure surface of Ganz (1985). Additionally, the model is not yet reasonably validated for horizontal and vertical tension, since no experimental data is available for vertically perforated clay block masonry. Thus, an experimental campaign would be necessary to validate the model for these loading states. Another interesting modification to consider is the use of the phase field method (see, e. g., Miehe et al. (2010)), as a substitute for the XFEM approach. The phase field method is known to be very stable, even for complex crack topologies, as, e. g., Pech et al. (2022a,b) showed for wood, and could therefore enable the investigation of the post-peak behavior of vertically perforated clay block masonry in more detail. Finally, the model could also be validated for masonry glued with polyurethane adhesive in the bed joints, since this is a rising technology in the field of masonry construction and could be considered in the presented model with only minor adaptions.

CRediT authorship contribution statement

Raphael Reismüller: Writing – review & editing, Writing – original draft, Visualization, Validation, Resources, Methodology, Investigation, Formal analysis, Data curation, Conceptualization. **Markus Lukacevic:** Writing – review & editing, Supervision, Methodology, Conceptualization. **Sebastian Pech:** Writing – review & editing, Methodology, Conceptualization. **Andreas Jäger:** Writing – review & editing, Project administration, Funding acquisition, Conceptualization. **Josef Füssl:** Writing – review & editing, Supervision, Project administration, Methodology, Funding acquisition, Conceptualization.

Declaration of competing interest

The authors declare that they have no known competing financial interests or personal relationships that could have appeared to influence the work reported in this paper.

Data availability

Data will be made available on request.

Declaration of generative AI and AI-assisted Technologies in the writing process

During the preparation of this work the authors used ChatGPT and Github Copilot in order to improve the readability of the manuscript. After using these tools, the authors reviewed and edited the content as needed and take full responsibility for the content of the publication.

Acknowledgments

The authors gratefully acknowledge the financial support of the Austrian Research Promotion Agency (FFG, project number 865067) and the industry partner Wienerberger for funding the research work within the project “Innovative Brick 2”. Furthermore, the authors acknowledge TU Wien Bibliothek, Austria for financial support through its Open Access Funding Programme.

Appendix A. Failure criteria after Ganz

In the following, the 12 failure criteria after Ganz (1985) are presented. Note, that the indices are different than in the original publication. While Ganz (1985) refers to the vertical direction with x and to the horizontal direction with y, we use x for the horizontal direction and z for the vertical direction.

A.1. Block failure

$$\Phi_{1a} = \tau_{xz}^2 - \left(\omega_m \cdot f_{m,x} - \sigma_{xx}\right)\left(2\omega_m \cdot f_{m,z} - \sigma_{zz}\right) \leq 0. \tag{A.1}$$

$$\Phi_{1b} = \left(1 + \omega_m\right)^2 \cdot \tau_{xz}^2 + \left[\omega_m \cdot \left(\sigma_{zz} + f_{m,z}\right) - \sigma_{xx}\right] \times \left[\sigma_{zz} + f_{m,z} - f_{m,x} - \omega_m \cdot \left(\sigma_{xx} + f_{m,x}\right)\right] \leq 0. \tag{A.2}$$

$$\Phi_{1c} = \left(1+\omega_m\right)^2 \cdot \bar{\sigma}_{xz}^2 + \left[\omega_m \cdot \left(\bar{\sigma}_{zz} - 2\omega_m \cdot f_{m,z} + f_{m,x} \cdot \left(1+\omega_m\right)\right) - \bar{\sigma}_{xx}\right] \cdot \left[\bar{\sigma}_{zz} - 2\omega_m \cdot f_{m,z} - \omega_m \cdot f_{m,x}\right] \leq 0. \tag{A.3}$$

$$\Phi_2 = \tau_{xz}^2 - \left(\sigma_{xx} + f_{m,x}\right) \cdot \left(\sigma_{zz} + f_{m,z}\right) \leq 0. \tag{A.4}$$

$$\Phi_{3ab} = \tau_{xz}^2 + \sigma_{xx} \cdot \left(\sigma_{xx} + f_{m,x}\right) \leq 0. \tag{A.5}$$

$$\Phi_{3c} = \tau_{xz}^2 + \left(\sigma_{xx} - \omega_m \cdot f_{m,x} + R_a\right)^2 - R_a^2 \leq 0. \tag{A.6}$$

$$R_a = d \cdot \tan\left(\frac{\pi}{4} - \frac{\tan^{-1}(k)}{2}\right) - f_{m,x} \cdot \frac{1-\omega_m}{2} \quad \text{where } d = \frac{\omega_m \cdot f_{m,x}}{2 \cdot \sqrt{\omega_m}} \text{ and } k = \frac{\omega_m - 1}{2 \cdot \sqrt{\omega_m}} \tag{A.7}$$

$$\Phi_{3d} = 4\omega_m \cdot \tau_{xz}^2 - \left[\omega_m \cdot f_{m,x} - \sigma_{xx} \cdot \left(1-\omega_m\right)\right]^2 \leq 0. \tag{A.8}$$

A.2. Mortar joint failure

$$\Phi_{4a} = \tau_{xz}^2 - \left(c - \sigma_{zz} \cdot \tan(\varphi)\right)^2 \leq 0. \tag{A.9}$$

$$\Phi_{4b} = \tau_{xz}^2 + \left(\sigma_{zz} - f_{t,z} + R_b\right)^2 - R_b^2 \leq 0. \tag{A.10}$$

$$\Phi_{4c} = \tau_{xz}^2 + \left[\sigma_{zz} - f'_{t,z} \cdot \left(\frac{\sigma_{xx}}{\mu \cdot f_{m,x}} + 1\right) + R_c\right]^2 - R_c^2 \leq 0. \tag{A.11}$$

$$\Phi_{4d} = \tau_{xz}^2 \cdot \left(1 + \frac{2 \cdot a_L}{a_S} \cdot \tan(\varphi)\right)^2 - \left(\sigma_{zz} \cdot \tan(\varphi) + \sigma_{xx} \cdot \frac{2 \cdot a_L}{a_s} - c\right)^2 \leq 0. \tag{A.12}$$

$$\Phi_{4e} = \left(|\tau_{xz}| + \frac{2a_L}{a_S} \cdot \sigma_{xx}\right)^2 + \left(\sigma_{zz} + |\tau_{xz}| \cdot \frac{2a_L}{a_S} - f_{t,z} + R_b\right)^2 - R_b^2 \leq 0. \tag{A.13}$$

$$R_b = c \cdot \tan\left(\frac{\pi}{4} + \frac{\varphi}{2}\right) - f_{t,z} \cdot \frac{\sin(\varphi)}{1-\sin(\varphi)} \tag{A.14}$$

$$R_c = c \cdot \tan\left(\frac{\pi}{4} + \frac{\varphi}{2}\right) - f'_{t,z} \cdot \left(\frac{\sigma_{xx}}{\mu \cdot f_{m,x}} + 1\right) \cdot \frac{\sin(\varphi)}{1-\sin(\varphi)} \tag{A.15}$$

Note, that the equation for failure criterion 3c in the original publication seems to be wrong, since it always indicates failure at $\sigma_{xx} \geq 0$, although horizontal tensile stresses should be possible. Using the verbal description of Ganz (1985), a new criterion was defined, assuming the surface to describe a cylinder (see Eq. (A.6)). The original equation in the publication is the following:

$$\Phi_{3c,o} = \tau_{xz}^2 + \sigma_{xx} \cdot \left(\sigma_{xx} - \omega_m \cdot f_{m,x}\right) \leq 0. \tag{A.16}$$

Appendix B. Rankine–Hill surface

The Rankine-type surface is defined in the following manner:

$$f_1 = \frac{(\sigma_x - f_{t,x}) + (\sigma_z - f_{t,z})}{2} + \sqrt{\left(\frac{(\sigma_x - f_{t,x}) - (\sigma_z - f_{t,z})}{2}\right)^2 + \alpha\tau_{xz}^2} = 0, \tag{B.1}$$

with the parameter α, which is derived from the uniaxial tensile strengths, $f_{t,x}$ and $f_{t,z}$, as well as the pure shear strength of the material, τ_u as follows:

$$\alpha = \frac{f_{t,x} \cdot f_{t,z}}{\tau_u}. \tag{B.2}$$

The Hill-type surface forms a rotated centered ellipsoid, which reads as

$$f_2 = A \cdot \sigma_x^2 + B \cdot \sigma_x \cdot \sigma_z + C \cdot \sigma_z^2 + D \cdot \tau_{xz}^2 - 1 = 0. \tag{B.3}$$

The four parameters A, B, C, and D can be derived from the material strengths an equivalent yield stresses in the following way:

$$A = \frac{1}{\left(f_{m,x}\right)^2},\ B = \frac{\beta}{f_{m,x} \cdot f_{m,z}},\ C = \frac{1}{\left(f_{m,z}\right)^2},\ \text{and } D = \frac{\gamma}{f_{m,x} \cdot f_{m,z}}. \tag{B.4}$$

Appendix C. Supplementary data

Supplementary material related to this article can be found online at https://doi.org/10.1016/j.euromechsol.2024.105295.

References

Andreaus, U., 1996. Failure criteria for masonry panels under in-plane loading. J. Struct. Eng. 122 (1), 37–46. http://dx.doi.org/10.1061/(ASCE)0733-9445(1996)122:1(37).

Anthoine, A., 1995. Derivation of the in-plane elastic characteristics of masonry through homogenization theory. Int. J. Solids Struct. 32 (2), 137–163. http://dx.doi.org/10.1016/0020-7683(94)00140-R.

Belytschko, T., Black, T., 1999. Elastic crack growth in finite elements with minimal remeshing. Internat. J. Numer. Methods Engrg. 45 (5), 601–620. http://dx.doi.org/10.1002/(SICI)1097-0207(19990620)45:5<601::AID-NME598>3.0.CO;2-S.

Bitterli, S., 2014. Versuche an Mauerwerkselementen mit geneigten Lagerfugen. (Master's thesis). ETH Zürich, Zürich, URL: https://ethz.ch/content/dam/ethz/special-interest/baug/ibk/structural-masonry-dam/education/MS_Thesis_Bitterli.pdf.

Bocca, P., Carpinteri, A., Valente, S., 1989. Fracture mechanics of brick masonry: Size effects and snap-back analysis. Mater. Struct. 22 (5), 364–373. http://dx.doi.org/10.1007/BF02472507.

Böhm, H.J., 2023. A short introduction to basic aspects of continuum micromechanics. ILSB Rep. URL: https://www.ilsb.tuwien.ac.at/links/downloads/ilsbrep206.pdf.

Bošnjak, J., Gambarelli, S., Sharma, A., Mešković, A., 2020. Experimental and numerical studies on masonry after exposure to elevated temperatures. Constr. Build. Mater. 230, 116926. http://dx.doi.org/10.1016/j.conbuildmat.2019.116926.

Buchner, T., Königsberger, M., Jäger, A., Füssl, J., 2022. A validated multiscale model linking microstructural features of fired clay brick to its macroscopic multiaxial strength. Mech. Mater. 170, 104334. http://dx.doi.org/10.1016/j.mechmat.2022.104334.

Da Porto, F., Guidi, G., Garbin, E., Modena, C., 2010. In-plane behavior of clay masonry walls: Experimental testing and finite-element modeling. J. Struct. Eng. 136 (11), 1379–1392. http://dx.doi.org/10.1061/(ASCE)ST.1943-541X.0000236, URL: https://ascelibrary.org/doi/10.1061/%28ASCE%29ST.1943-541X.0000236.

Dassault Systèmes, 2022. Abaqus Online Documentation. URL: https://help.3ds.com/2022/English/DSSIMULIA_Established/SIMULIA_Established_FrontmatterMap/sim-r-DSDocAbaqus.htm?contextscope=all.

Dialer, C., 1990. Bruch- und Verformungsverhalten von schubbeanspruchten Mauerwerksscheiben, zweiachsige Versuche an verkleinertem Modellmauerwerk (Ph.D. thesis). TU München, München.

Dlubal Software GmbH, 2020. Masonry Design using the Rankine–Hill failure surface. URL: https://www.dlubal.com/en/products/add-ons-for-rfem-6-and-rstab-9/design/masonry-design.

Eis, A., Vassilev, T., 2013. Übersicht über abgeschlossene und laufende Forschungsvorhaben im Mauerwerksbau. In: Jäger, W. (Ed.), Mauerwerk-Kalender 2012. Wiley, Weinheim, Germany, pp. 609–647. http://dx.doi.org/10.1002/9783433601617.ch17.

EN 1052-1, 1998. Methods of Test for Masonry - Part 1: Determination of Compressive Strength. CEN — European Committee for Standardization, Brussels, BEL.

EN 1052-3, 2002. Methods of Test for Masonry - Part 3: Determination of Initial Shear Strength. CEN — European Committee for Standardization, Brussels, BEL.

EN 772-1, 2016. Methods of Test for Masonry Units - Part 1: Determination of Compressive Strength. CEN — European Committee for Standardization, Brussels, BEL.

Essawy, A.S., Drysdale, R.G., 1986. Macroscopic failure criterion for masonry assemblages. In: Proceedings of the 4th Canadian Masonry Symposium, Fredericton, NB, Canada.

Gaetano, D., Greco, F., Leonetti, L., Lonetti, P., Pascuzzo, A., Ronchei, C., 2022. An interface-based detailed micro-model for the failure simulation of masonry structures. Eng. Fail. Anal. 142, 106753. http://dx.doi.org/10.1016/j.engfailanal.2022.106753.

Ganz, H.R., 1985. Mauerwerksscheiben unter Normalkraft und Schub (Ph.D. thesis). ETH Zurich, p. 133. http://dx.doi.org/10.3929/ETHZ-A-000360363, URL: http://hdl.handle.net/20.500.11850/138655.

Ganz, H.R., Thürlimann, B., 1982. Versuche über die Festigkeit von zweiachsig beanspruchtem Mauerwerk. p. 61 S.. http://dx.doi.org/10.3929/ETHZ-A-000248407.

Grande, E., Imbimbo, M., Sacco, E., 2013. Finite element analysis of masonry panels strengthened with FRPs. Composites B 45 (1), 1296–1309. http://dx.doi.org/10.1016/j.compositesb.2012.09.002.

Grande, E., Milani, G., Sacco, E., 2008. Modelling and analysis of FRP-strengthened masonry panels. Eng. Struct. 30 (7), 1842–1860. http://dx.doi.org/10.1016/j.engstruct.2007.12.007.

Hamid, A.A., Drysdale, R.G., 1981. Proposed failure criteria for concrete block masonry under biaxial stresses. J. Struct. Div. 107 (8), 1675–1687. http://dx.doi.org/10.1061/JSDEAG.0005772.

Hannawald, J., 2006. Determining the tensile softening diagram of concrete-like materials using hybrid optimisation. In: Konsta-Gdoutos, M.S. (Ed.), Measuring, Monitoring and Modeling Concrete Properties. Springer Netherlands, Dordrecht, pp. 179–187. http://dx.doi.org/10.1007/978-1-4020-5104-3_22.

Hegemier, G.A., Arya, S., Krishnamoorthy, G., Nachbar, W., Furgeson, R., 1978. On the behavior of joints in concrete masonry. In: Proc. North American Conference, Masonry Society, USA.

Hendry, A.W., 1978. A note on the strength of brickwork in combined racking shear and compression. In: Proceeding of the British Ceramic Society. volume 27, pp. 47–52.

Hoffman, O., 1967. The brittle strength of orthotropic materials. J. Compos. Mater. 1 (2), 200–206. http://dx.doi.org/10.1177/002199836700100210.

Jafari, S., Rots, J.G., Esposito, R., 2019. Core testing method to assess nonlinear behavior of brick masonry under compression: A comparative experimental study. Constr. Build. Mater. 218, 193–205. http://dx.doi.org/10.1016/j.conbuildmat.2019.04.188.

Kiefer, T., Kariem, H., Lukacevic, M., Füssl, J., 2017. The compressive strength of vertically perforated clay block masonry predicted by means of a unit-cell type numerical simulation tool taking discrete cracking into account. Constr. Build. Mater. 150, 24–34. http://dx.doi.org/10.1016/j.conbuildmat.2017.05.201.

Kotze, M., Van Rooyen, G.C., Van Zijl, G.P.A.G., 2019. Retrofitting unreinforced masonry buildings with a strain-hardening cement-based composite to enhance seismic resistance. In: Proceedings of the 10th International Conference on Fracture Mechanics of Concrete and Concrete Structures. IA-FraMCoS, http://dx.doi.org/10.21012/FC10.233248, URL: https://framcos.org/FraMCoS-10/Full-Papers/233248.pdf.

Lang, K., Bachmann, H., 2003. On the seismic vulnerability of existing unreinforced masonry buildings. J. Earthq. Eng. 7 (3), 407–426. http://dx.doi.org/10.1080/13632460309350456, URL: http://www.tandfonline.com/doi/full/10.1080/13632460309350456.

Leonetti, L., Greco, F., Trovalusci, P., Luciano, R., Masiani, R., 2018. A multiscale damage analysis of periodic composites using a couple-stress/Cauchy multidomain model: Application to masonry structures. Composites B 141, 50–59. http://dx.doi.org/10.1016/j.compositesb.2017.12.025.

Lourenço, P.B., 1996. Computational Strategies for Masonry Structures (Ph.D. thesis). Delft University of Technology, URL: http://resolver.tudelft.nl/uuid:4f5a2c6c-d5b7-4043-9d06-8c0b7b9f1f6f.

Lourenço, P.B., De Borst, R., Rots, J.G., 1997. A plane stress softening plasticity model for orthotropic materials. Internat. J. Numer. Methods Engrg. 40 (21), 4033–4057. http://dx.doi.org/10.1002/(SICI)1097-0207(19971115)40:21<4033::AID-NME248>3.0.CO;2-0, URL: https://onlinelibrary.wiley.com/doi/10.1002/(SICI)1097-0207(19971115)40:21<4033::AID-NME248>3.0.CO;2-0.

Mann, W., Müller, H., 1982. Failure of shear-stressed masonry: An enlarged theory, tests and application to shear walls. In: Proceeding of the British Ceramic Society. volume 30, pp. 223–235.

McKay, M.D., Beckman, R.J., Conover, W.J., 1979. Comparison of three methods for selecting values of input variables in the analysis of output from a computer code. Technometrics 21 (2), 239–245. http://dx.doi.org/10.1080/00401706.1979.10489755.

Miehe, C., Hofacker, M., Welschinger, F., 2010. A phase field model for rate-independent crack propagation: Robust algorithmic implementation based on operator splits. Comput. Methods Appl. Mech. Engrg. 199 (45), 2765–2778. http://dx.doi.org/10.1016/j.cma.2010.04.011.

Mistler, M., Butenweg, C., Meskouris, K., 2006. Modelling methods of historic masonry buildings under seismic excitation. J. Seismol. 10 (4), 497–510. http://dx.doi.org/10.1007/s10950-006-9033-z, URL: http://link.springer.com/10.1007/s10950-006-9033-z.

Mojsilović, N., 1995. Zum Tragverhalten von kombiniert beanspruchtem Mauerwerk (Ph.D. thesis). ETH Zurich, p. 130. http://dx.doi.org/10.3929/ETHZ-A-001549685, URL: http://hdl.handle.net/20.500.11850/142387.

Mojsilović, N., 2011. Strength of masonry subjected to in-plane loading: A contribution. Int. J. Solids Struct. 48 (6), 865–873. http://dx.doi.org/10.1016/j.ijsolstr.2010.11.019.

Netzel, H., Van Zijl, G.P.A.G., 2004. Nonlinear numerical simulation of settlement-induced damage to solid masonry walls. In: Proceedings of the 13th International Brick and Block Masonry Conference. URL: https://citeseerx.ist.psu.edu/document?repid=rep1&type=pdf&doi=5b9f71945957bd2dfedb9052b81967197adacd4c.

Page, A.W., 1981. The biaxial compressive strength of brick masonry. Proc. Inst. Civ. Eng. (71), 893–906.

Page, A.W., 1983. The strength of brick masonry under biaxial tension-compression. Int. J. Mason. Constr. 3 (1), 26–31.

Pech, S., Lukacevic, M., Füssl, J., 2022a. A hybrid multi-phase field model to describe cohesive failure in orthotropic materials, assessed by modeling failure mechanisms in wood. Eng. Fract. Mech. 271, 108591. http://dx.doi.org/10.1016/j.engfracmech.2022.108591.

Pech, S., Lukacevic, M., Füssl, J., 2022b. Validation of a hybrid multi-phase field model for fracture of wood. Eng. Fract. Mech. 275, 108819. http://dx.doi.org/10.1016/j.engfracmech.2022.108819.

Pohl, S., 2020. Beitrag des Mauerwerksbaus zum nachhaltigen Bauen. Mauerwerk 24 (2), 100–107. http://dx.doi.org/10.1002/dama.202000003.

Reismüller, R., Königsberger, M., Jäger, A., Füssl, J., 2023a. The performance of vertically perforated clay block masonry in fire tests predicted by a finite-element model including an energy-based criterion to identify spalling. Fire Saf. J. 135, 103729. http://dx.doi.org/10.1016/j.firesaf.2022.103729.

Reismüller, R., Lukacevic, M., Pech, S., Jäger, A., Füssl, J., 2023b. A numerical unit cell model for predicting the failure stress state of vertically perforated clay block masonry under arbitrary in-plane loads. Eng. Struct. 293, 116557. http://dx.doi.org/10.1016/j.engstruct.2023.116557.

Rudisch, A., Dunjic, V., Kolbitsch, A., 2017. Investigation of horizontal floor acceleration in historic masonry buildings: Untersuchung der horizontalen Stockwerksbeschleunigungen historischer Mauerwerksbauten. Mauerwerk 21 (6), 348–356. http://dx.doi.org/10.1002/dama.201700017, URL: https://onlinelibrary.wiley.com/doi/10.1002/dama.201700017.

Salmanpour, A.H., 2017. Displacement Capacity of Structural Masonry (Ph.D. thesis). ETH Zurich, p. 148. http://dx.doi.org/10.3929/ETHZ-B-000172566.

Scacco, J., Ghiassi, B., Milani, G., Lourenço, P.B., 2020. A fast modeling approach for numerical analysis of unreinforced and FRCM reinforced masonry walls under out-of-plane loading. Composites B 180, 107553. http://dx.doi.org/10.1016/j.compositesb.2019.107553.

Scacco, J., Grillanda, N., Milani, G., Lourenço, P.B., 2022. Novel non-linear static numerical model for curved masonry structures based on a combined adaptive limit analysis and discrete FE computations. Int. J. Solids Struct. 236–237, 111265. http://dx.doi.org/10.1016/j.ijsolstr.2021.111265.

Schlegel, R., Rautenstrauch, K., 2000. Ein elastoplastisches berechnungsmodell Zur Räumlichen untersuchung von mauerwerkstrukturen. Bautechnik 77 (6), 426–436. http://dx.doi.org/10.1002/bate.200003100.

Segura, J., Pelà, L., Saloustros, S., Roca, P., 2021. Experimental and numerical insights on the diagonal compression test for the shear characterisation of masonry. Constr. Build. Mater. 287, 122964. http://dx.doi.org/10.1016/j.conbuildmat.2021.122964.

Seim, W., 1995. Numerische modellierung des anisotropen versagens zweiachsig beanspruchter mauerwerksscheiben.

Seim, W., Pfeiffer, U., 2011. Local post-strengthening of masonry structures with fiber-reinforced polymers (FRPs). Constr. Build. Mater. 25 (8), 3393–3403. http://dx.doi.org/10.1016/j.conbuildmat.2011.03.030, URL: https://linkinghub.elsevier.com/retrieve/pii/S0950061811000766.

Suda, R., Kiefer, T., Schranz, C., Füssl, J., 2021. A finite-element-based approach to quantify the impact of bed joint reinforcement on the compressive strength of vertically perforated clay block masonry. Eng. Struct. 239, 112277. http://dx.doi.org/10.1016/j.engstruct.2021.112277.

Van Den Heever, M., Bester, F., Kruger, J., Van Zijl, G., 2021. Mechanical characterisation for numerical simulation of extrusion-based 3D concrete printing. J. Build. Eng. 44, 102944. http://dx.doi.org/10.1016/j.jobe.2021.102944, URL: https://linkinghub.elsevier.com/retrieve/pii/S2352710221008020.

Van der Pluijm, R., 1999. Out-of-Plane Bending of Masonry : Behaviour and Strength (Ph.D. thesis). Technische Universiteit Eindhoven, URL: https://research.tue.nl/en/publications/out-of-plane-bending-of-masonry-behaviour-and-strength.

Vratsanou, V., 1992. Das nichtlineare verhalten unbewehrter mauerwerksscheiben unter erdbebenbeanspruchung. Hilfsmittel zur Bestimmung der q-Faktoren. Diss. Univ. Karlsruhe.

Wan, Q., Yi, W., 1986. The shear strength of masonry wall under combined stresses. In: Proceedings of the Fourth Canadian Masonry Symposium. University of New Brunswick, Canada.

Wienerberger, A.G., 2023. Porotherm S9 36,5 MW. URL: https://www.wienerberger.de/produkte/wand/ziegel/poroton-s9-36,5-miwo.html.

Zhou, Y., Sluys, L.J., Esposito, R., 2022. An improved mean-field homogenization model for the three-dimensional elastic properties of masonry. Eur. J. Mech. A Solids 96, 104721. http://dx.doi.org/10.1016/j.euromechsol.2022.104721.

Zilch, K., Schermer, D., 2003. Untersuchungen zum verhalten von mauerwerksgebäuden unter erdbebenbeanspruchung. Bauingenieur 78 (7), 360–368.

Zürcher Ziegeleien, A.G., 2023. SwissModul 15. URL: https://www.zz-ag.ch/produkte/wand/mauerwerk/swissmodul-15.html.